https://dx.doi.org/10.1016/j.jcsr.2016.11.023

DIRECT ANALYSIS OF HIGH-STRENGTH CONCRETE-FILLED-TUBULAR COLUMNS WITH CIRCULAR & OCTAGONAL SECTIONS

by

Si-Wei Liu, Tak-Ming Chan, Siu-Lai Chan* and Derek Kwok-Leung So

Department of Civil and Environmental Engineering, The Hong Kong Polytechnic University, Hung Hom, Kowloon, Hong Kong, China

Author Affiliations:

[1]*Research Fellow, Department of Civil and Environmental Engineering, The Hong Kong Polytechnic University, Hung Hom, Kowloon, Hong Kong, China, E-mail: siwei.liu@connect.polyu.hk*

[2] *Assistant Professor, Department of Civil and Environmental Engineering, The Hong Kong Polytechnic University, Hung Hom, Kowloon, Hong Kong, China, E-mail: tak-ming.chan@polyu.edu.hk*

[3]*Chair Professor, Department of Civil and Environmental Engineering, The Hong Kong Polytechnic University, Hung Hom, Kowloon, Hong Kong, China,* ***(corresponding author)*** *E-mail: ceslchan@polyu.edu.hk*

[4]*Executive Director, Hip Hing Construction Co. Ltd., E-mail: derek_so@hiphing.com.hk*

Abstract

High-strength-concrete (HSC) is brittle, but its ductility can be dramatically increased when confined by steel tubes. However, the size of hot-rolled tubular sections is commonly limited to 600mm, its capacity as mega columns in many high-rise buildings is inadequate. This paper details the use of fabricated and rolled sections as mega-columns by the direct analysis of design (DAM) which is further presented for application with high-strength-concrete-filled-tubular (HCFT) columns of circular and octagonal sections allowing for confinement effects in concrete. To capture the material yielding behaviors and to allow for an explicit simulation on the member initial curvatures, a curved-piecewise-Hermite(CPH) element is especially developed for simulating the behaviors of HCFT columns under extreme loading conditions. A plastic-fiber-hinge-model using the sectional strength-iteration surfaces is proposed for capturing the yielding behavior at the hinge locations and the analytical method for generating the yield surfaces is elaborated. To this, one-element-per-member is sufficient for numerical simulation; and the savings in computer time are considerable, making the proposed theory practical. The material model for the HSC in steel tubes is essential for a successful design. To this, an experiment on two groups of confined specimens, e.g. circular and octagonal, is established for investigating the properties of HSC, and an approximated calculation method is proposed and validated with the experiments. Consequently, the corresponding stress vs. strain relations of the confined HSC can be determined for use in analysis. Finally, examples are given for verifying and validating the proposed method for HCFT columns with circular and octagonal sections.

Keywords: *Direct Analysis; Element; High-strength concrete; Nonlinear; Octagonal; Steel*

1. Introduction

Direct analysis, which is also sometimes called as second-order plastic analysis with geometric and material imperfections, is advocated to investigate the true and ultimate structural behavior of members and frames over the past decades. This method is widely adopted in conventional structural design under static loads, performance-based seismic design, progressive collapse analysis and structural fire analysis. In order to reflect the actual structural performance and stability, the vital effects inherent to the members are needed to be considered and they include the large deflection effect, material yielding and initial member curvatures.

Concrete-filled tubular (CFT) columns are among the most economical and structurally efficient among reinforced and composite members in terms of resistance to high compressive loads. In addition to the steel tube being used as a load-carrying component, it also provides the confinement to the concrete core, thereby increases the compressive strength and improves ductility of the concrete. Further, the steel sections can be used as temporary works for fresh concrete so the cost of fabricating formworks can be saved. All these advantages are well-recognized and supported by experiments and reported (see, for example, Knowles and Park [1], Wardenier *et al.* [2] and Han *et al.* [3]). Extensive research and experiments have been conducted in the past decades to investigate the behaviors of CFT columns including Tomii *et al.* [4], Tanaka *et al.* [5], Schneider [6], Huang *et al.* [7], Mursi and Uy [8], Hu *et al.* [9], Dai and Lam [10], Sheehan *et al.* [11], Ellobody [12], Han *et al.* [3] and Dai *et al.* [13].

When using the structural form, a considerable increase in load bearing capacity due to concrete confinement effect is achieved and column size can be reduced with an increase in the usable floor area. Additionally, the concrete core restricts the local buckling of surrounding steel tubes and increases the column stiffness. Susantha *et al*. [14] investigated

the Hyogoken-Nanbu earthquake in Japan and noted another advantage of CFT columns as having more ductility and larger energy absorbing capacity than the bare steel or reinforced concrete columns. Summarizing all these observations, CFT columns are thus favorable structural components for tall buildings constructed in high-density urban areas and earthquake-active regions.

However, the commercial off-the-shelf tubular columns are limited to rectangular, circular and elliptical cross-section (see **Fig. 1**a to 1c). Their maximum outer diameter, *D* and thickness, *t* are normally less than 500 mm and 50 mm, respectively. For high-rise buildings less than 100 meters, tubular columns are normally fabricated as welded sections (see **Fig. 2**a) to increase the load-carrying capacity. In recent years, mega-size cross-sections as shown in **Fig. 3** have been adopted to further increase the load-carrying capacity for super high-rise buildings with height over 100 meters. As the maximum diameter of tubular sections is generally limited to 500mm, the size of using them as columns cannot satisfy the need for a column in a high rise building under high axial compression due to accumulative loads from floors above.

In addition to the load-carrying capacity, steel tube can also confine the concrete in-fill, and hence increases the compressive strength and significantly improves the ductility of the concrete. Research from Susantha *et al.* [15] indicated that this influence would be dramatically affected by the cross-section shape of the tube. The strength and ductility of the confined concrete core can be increased in circular CFT columns [1], while only the ductility of the concrete in CFT members with rectangular sections can be improved [16]. However, manufacturing challenges would be encountered while fabricating a large-sized circular steel tube. Therefore, an optimal and practical solution can be achieved by using the alternative – octagonal shaped section, as illustrated in **Fig. 2**b. It is crucial to investigate the corresponding confinement behavior on the concrete core in this octagonal shaped section.

In this research, high strength concrete (HSC) refers to concrete with the characteristic concrete cube strength greater than 60 MPa (~8.7 ksi). HSC offers greater stiffness and strength than normal strength concrete. To date, the readily-mixed product of HSC can be easily sourced in the market and is being extensively used [17]. However, HSC is an extremely brittle material as schematically shown in **Fig. 4**. Nevertheless, when it is confined by circular steel tubes, both the ductility and strength of HSC can be improved (see **Fig. 5**, Liew *et al.* [18]).

High-strength concrete-filled-tubular (HCFT) columns are usually slender and their stability problems are dominant and therefore the P-δ-Δ effects are important in design. To achieve an acceptable level of accuracy, the member local imperfection should be taken into account otherwise the structural stability cannot be assessed reliably. The curved high-order beam-column element developed by Chan and Zhou [19] and the curved stability function element proposed by Chan and Gu [20] are suitable candidates for analysis of slender axially-loaded members and also have been widely used in the design practice. However, the current theories mainly use the conventional refined plastic hinge method and it assumes the plastic hinges are formed only at the element ends. Therefore, two and more elements are required for accurate modeling of a member to capture the plastic hinge location. This not only increases the computational time, but also causes difficulties in modeling the member imperfections. In this paper, a curved-piecewise-Hermite (CPH) element is developed for simulating the HCFT columns with circular and octagonal sections, which is derived on the basis of the arbitrarily-located-hinge (ALH) element developed by Liu *et. al* [21, 22] and the work originally conducted by Chen and Chan [23] .

To reflect the inelastic behavior of HCFT columns, an approach using the plastic fiber hinge model [24] is adopted in the present study. Material yielding on hinge locations is reflected by a gradually softening spring. Contrary to the traditional or refined plastic hinge model,

where the simplified linear interaction equations are adopted to examine yielding on sections, the accurate and rigorous criterion described by the sectional yield surfaces are utilized in the proposed plastic fiber hinge model. To generate the sectional yield surfaces, the numerical method based on quasi-Newton interactive scheme [25] is employed, where the steel and concrete components are divided into several fibers and parallel layers, respectively, in calculating the stress resultants of a cross section.

The material constitutive relations are essential and vital for an accurate numerical simulation and the design by direct analysis. Many researchers proposed the stress vs. strain models for the confined concrete, such as Mander *et al.* [26], Cusson and Paultre [27], Susantha *et al.* [15], Binici [28], Lokuge *et al.* [29] and Samani and Attard [30]. In the present study, the stress vs. strain curve from Eurocode-2 [31] is employed for the confined high-strength concrete, where the effective confining stress is the crucial factor in the relation. The lateral pressure acting on the concrete core in a circular tubular section can be calculated by the force-equilibrium method to be discussed in the followings. However, research on the effective confining stress for the concrete in the octagonal tube is limited. This paper, proposes an effective confinement area method to approximate the confining stress and hence, to obtain the corresponding strain vs. strain curves for the confined high-strength concrete in circular and octagonal steel tubes.

To verify the proposed material models, an experimental investigation was carried out to study the behavior of confined high-strength concrete in tubular columns. Two comparison groups, which contained two circular and octagonal tubular specimens with the depth-to-thickness (d/t) ratio equaling to 38.74, were tested. Besides, another two groups of unconfined specimens, which had the same size of the concrete core in the confined specimens, were also examined. The stress vs. strain curves of the confined and unconfined

concrete were measured in the experiment, and the results were compared with the proposed material constitutive models.

Further, in this paper, a direct analysis method for HCFT columns is proposed, large deflection, imperfections, confinement effects and material yielding are all taken into consideration. A curved-piecewise-Hermite (CPH) element is developed and its formulations for the numerical analysis are elaborated. For capturing the yielding behavior at the hinge locations, a plastic fiber hinge model using the sectional yield surfaces is introduced. The sectional yield surfaces for the HCFT circular and octagonal sections are produced by a robust cross-section analysis technique. The material constitutive model for the confined high-strength concrete in the circular and octagonal steel tubes is proposed and verified by the experiment. Finally, for validating the accuracy, applicability and effectiveness of the proposed analytical model, several examples are solved.

2. Numerical Analysis Framework

2.1 Assumptions

In the current study, the following assumptions are adopted for the analysis of the HCFT columns and their cross sections. (1) Small strains but large deformations are assumed and handled using the incremental tangent stiffness method proposed by Chan [32]; (2) Euler-Bernoulli hypothesis is adopted and the strain distribution along the cross section is linear; (3) Second-order effects including the P-Δ and P-δ deformations and imperfections are considered; (4) Material yielding on the critical section is simulated by the plastic fibre hinge; (5) Loads are conservative and applied on element nodes; (6) Slippage between the steel tube and the concrete core is disregarded; and (7) Tensile strength of concrete is only taken into account in computing the concrete fracture surface and ignored in calculations at other limit states.

2.2 Element formulations

To simulate the behaviors of HCFT columns, the vital effects including initial imperfections, material yielding and large deformations, must be incorporated into the element formulations. To this, a beam-column element with the piecewise-Hermite shape functions and initial member curvature is proposed in the present study.

Referring to **Fig. 9**, there are twelve degrees of freedom (DOFs) for displacements and given by :

$$\{\mathrm{u}\} = \{e \quad \theta_{11y} \quad \theta_{11z} \quad \theta_{x} \quad \theta_{12y} \quad \theta_{12z} \quad \delta_{z} \quad \delta_{y} \quad \theta_{21y} \quad \theta_{21z} \quad \theta_{22y} \quad \theta_{22z}\}^{T} \quad (1)$$

The piecewise shape function is presented as:

$$\begin{aligned} &\text{when } -0.5 \le \frac{x}{L} \le 0 \\ &\qquad \mathrm{v}_y(\mathrm{x}) = \{N_L\} \cdot \{\theta_{11y} \quad \theta_{12y} \quad \delta_z\}^T \\ &\qquad \mathrm{v}_z(\mathrm{x}) = \{N_R\} \cdot \{\theta_{11z} \quad \theta_{12z} \quad \delta_y\}^T \\ &\text{when } 0 \le \frac{x}{L} \le +0.5 \\ &\qquad \mathrm{v}_y(\mathrm{x}) = \{N_L\} \cdot \{\theta_{21y} \quad \theta_{22y} \quad \delta_z\}^T \\ &\qquad \mathrm{v}_z(\mathrm{x}) = \{N_R\} \cdot \{\theta_{21z} \quad \theta_{22z} \quad \delta_y\}^T \end{aligned} \quad (2)$$

where, the shape function vectors $\{N_L\}$ and $\{N_R\}$ are written as:

$$\{N_L\} = \{2x^2L(L+2x) \quad xL(L+2x)^2 \quad (L-4x)(L+2x)^2\}/L^3 \quad (3)$$

$$\{N_R\} = \{xL(L-2x)^2 \quad 2x^2L(L-2x) \quad (L+4x)(L-2x)^2\}/L^3 \quad (4)$$

The initial member imperfections can be incorporated by the parabolic equations as:

$$v_{oy}(x) = v_{moy}(1-(2x/L)^2) \text{ and } v_{oz}(x) = v_{moz}(1-(2x/L)^2) \quad (5)$$

in which, v_{moy} and v_{moz} are the magnitudes of the initial member imperfection at the mid-span for minor and major axes, respectively.

In the Finite Element Method (FEM), the secant relation and tangent stiffness matrix are required to be formulated for the incremental-iterative numerical procedure. To this, the total potential energy can be formulated as:

$$U = \frac{1}{2}\int_L EAu(\dot{x})^2 dx + \frac{1}{2}\int_L EI_y v_y(\ddot{x})^2 dx + \frac{1}{2}\int_L EI_z v_z(\ddot{x})^2 dx + \frac{1}{2}\int_L GJt(\dot{x})^2 dx \quad (6)$$

$$+\frac{1}{2}\int_L P(\dot{v_y}(x)^2 + 2\dot{v_{0y}}(x)\dot{v_y}(x))dx + \frac{1}{2}\int_L P(\dot{v_z}(x)^2 + 2\dot{v_{0z}}(x)\dot{v_z}(x))dx$$

$$+\int_{\theta_{my}} S_{my}d\theta + \int_{\theta_{mz}} S_{mz}d\theta$$

in which, $u(x)$ and $t(x)$ are the linear interpolation functions for the axial and torsional directions, respectively; θ_{my}, θ_{mz}, S_{my} and S_{mz} are the rotations and rigidities of the internal hinge at the mid-span for both axes.

The secant relations can be obtained by the first derivation of the total potential energy given by :

$$\begin{aligned}
\mathrm{P} &= \frac{\mathrm{EA}}{L}e + \frac{12\mathrm{EA}}{5L^2}{\delta_\mathrm{y}}^2 + \frac{12\mathrm{EA}}{5L^2}{\delta_\mathrm{z}}^2 + \frac{\mathrm{EA}}{30}{\theta_{11\mathrm{y}}}^2 + \frac{\mathrm{EA}}{30}{\theta_{11\mathrm{z}}}^2 + \left(-\frac{\mathrm{EA}}{6L}\mathrm{v_{m0y}} - \frac{\mathrm{EA}}{10L}\delta_\mathrm{z}\right)\theta_{12\mathrm{y}} + \frac{\mathrm{EA}}{30}{\theta_{12\mathrm{y}}}^2 \\
&+\theta_{11\mathrm{y}}\left(\frac{\mathrm{EA}}{6L}\mathrm{v_{m0y}} - \frac{\mathrm{EA}}{10L}\delta_\mathrm{z} - \frac{\mathrm{EA}}{60}\theta_{12\mathrm{y}}\right) + \left(-\frac{\mathrm{EA}}{6L}\mathrm{v_{m0z}} - \frac{\mathrm{EA}}{10L}\delta_\mathrm{y}\right)\theta_{12\mathrm{z}} + \frac{\mathrm{EA}}{30}{\theta_{12\mathrm{z}}}^2 \\
&+\theta_{11\mathrm{z}}\left(\frac{\mathrm{EA}}{6L}\mathrm{v_{m0z}} - \frac{\mathrm{EA}}{10L}\delta_\mathrm{y} - \frac{\mathrm{EA}}{60}\theta_{12\mathrm{z}}\right) + \frac{\mathrm{EA}}{30}{\theta_{21\mathrm{y}}}^2 + \frac{\mathrm{EA}}{30}{\theta_{21\mathrm{z}}}^2 - \frac{\mathrm{EA}}{6L}\mathrm{v_{m0y}}\theta_{22\mathrm{y}} + \frac{\mathrm{EA}}{30}{\theta_{22\mathrm{y}}}^2 \\
&+\theta_{21\mathrm{y}}\left(\frac{\mathrm{EA}}{6L}\mathrm{v_{m0y}} - \frac{\mathrm{EA}}{60}\theta_{22\mathrm{y}}\right) + \delta_\mathrm{z}\left(\frac{4\mathrm{EA}}{L^2}\mathrm{v_{m0y}} + \frac{\mathrm{EA}}{10L}\theta_{21\mathrm{y}} + \frac{\mathrm{EA}}{10L}\theta_{22\mathrm{y}}\right) - \frac{\mathrm{EA}}{6L}\mathrm{v_{m0z}}\theta_{22\mathrm{z}} + \frac{\mathrm{EA}}{30}{\theta_{22\mathrm{z}}}^2 \\
&+\theta_{21\mathrm{z}}\left(\frac{\mathrm{EA}}{6L}\mathrm{v_{m0z}} - \frac{\mathrm{EA}}{60}\theta_{22\mathrm{z}}\right) + \delta_\mathrm{y}\left(\frac{4\mathrm{EA}}{L^2}\mathrm{v_{m0z}} + \frac{\mathrm{EA}}{10L}\theta_{21\mathrm{z}} + \frac{\mathrm{EA}}{10L}\theta_{22\mathrm{z}}\right)
\end{aligned} \tag{7}$$

$$\mathrm{M_{11y}} = \frac{8\mathrm{EI_y}}{L}\theta_{11\mathrm{y}} + \frac{4\mathrm{EI_y}}{L}\theta_{12\mathrm{y}} - \frac{24\mathrm{EI_y}}{L^2}\delta_\mathrm{z} + \frac{LP}{15}\theta_{11\mathrm{y}} - \frac{LP}{60}\theta_{12\mathrm{y}} - \frac{P}{10}\delta_\mathrm{z} + \frac{P}{6}\mathrm{v_{m0y}} \tag{8}$$

$$\mathrm{M_{11z}} = \frac{8\mathrm{EI_z}}{L}\theta_{11\mathrm{z}} + \frac{4\mathrm{EI_z}}{L}\theta_{12\mathrm{z}} - \frac{24\mathrm{EI_z}}{L^2}\delta_\mathrm{y} + \frac{LP}{15}\theta_{11\mathrm{z}} - \frac{LP}{60}\theta_{12\mathrm{z}} - \frac{P}{10}\delta_\mathrm{y} + \frac{P}{6}\mathrm{v_{m0z}} \tag{9}$$

$$\mathrm{M_{12y}} = \frac{4\mathrm{EI_y}}{L}\theta_{11\mathrm{y}} + \frac{8\mathrm{EI_y}}{L}\theta_{12\mathrm{y}} - \frac{24\mathrm{EI_y}}{L^2}\delta_\mathrm{z} - \frac{LP}{60}\theta_{11\mathrm{y}} + \frac{LP}{15}\theta_{12\mathrm{y}} - \frac{P}{10}\delta_\mathrm{z} - \frac{P}{6}\mathrm{v_{m0y}} \tag{10}$$

$$\mathrm{M_{12z}} = \frac{4\mathrm{EI_z}}{L}\theta_{11\mathrm{z}} + \frac{8\mathrm{EI_z}}{L}\theta_{12\mathrm{z}} - \frac{24\mathrm{EI_z}}{L^2}\delta_\mathrm{y} - \frac{LP}{60}\theta_{11\mathrm{z}} + \frac{LP}{15}\theta_{12\mathrm{z}} - \frac{P}{10}\delta_\mathrm{y} - \frac{P}{6}\mathrm{v_{m0z}} \tag{11}$$

$$\mathrm{F_z} = \frac{24\mathrm{EI_y}}{L^3}\left[8\delta_\mathrm{z} + L\left(-\theta_{11\mathrm{y}} - \theta_{12\mathrm{y}} + \theta_{21\mathrm{y}} + \theta_{22\mathrm{y}}\right)\right] + \frac{P}{10L}\left[48\delta_\mathrm{z} + L\left(-\theta_{11\mathrm{y}} - \theta_{12\mathrm{y}} + \theta_{21\mathrm{y}} + \theta_{22\mathrm{y}}\right) + 40\mathrm{v_{m0y}}\right] \tag{12}$$

$$\mathrm{F_y} = \frac{24\mathrm{EI_z}}{L^3}\left[8\delta_\mathrm{y} + L(-\theta_{11\mathrm{z}} - \theta_{12\mathrm{z}} + \theta_{21\mathrm{z}} + \theta_{22\mathrm{z}})\right] + \frac{P}{10L}\left[48\delta_\mathrm{y} + L(-\theta_{11\mathrm{z}} - \theta_{12\mathrm{z}} + \theta_{21\mathrm{z}} + \theta_{22\mathrm{z}}) + 40\mathrm{v_{m0z}}\right] \tag{13}$$

$$\mathrm{M_{21y}} = \frac{8\mathrm{EI_y}}{L}\theta_{21\mathrm{y}} + \frac{4\mathrm{EI_y}}{L}\theta_{22\mathrm{y}} + \frac{24\mathrm{EI_y}}{L^2}\delta_\mathrm{z} + \frac{LP}{15}\theta_{21\mathrm{y}} - \frac{LP}{60}\theta_{22\mathrm{y}} + \frac{P}{10}\delta_\mathrm{z} + \frac{P}{6}\mathrm{v_{m0y}} \tag{14}$$

$$\mathrm{M_{21z}} = \frac{8\mathrm{EI_z}}{L}\theta_{21\mathrm{z}} + \frac{4\mathrm{EI_z}}{L}\theta_{22\mathrm{z}} + \frac{24\mathrm{EI_z}}{L^2}\delta_\mathrm{y} + \frac{LP}{15}\theta_{21\mathrm{z}} - \frac{LP}{60}\theta_{22\mathrm{z}} + \frac{P}{10}\delta_\mathrm{y} + \frac{P}{6}\mathrm{v_{m0z}} \tag{15}$$

$$\mathrm{M_{22y}} = \frac{4\mathrm{EI_y}}{L}\theta_{21\mathrm{y}} + \frac{8\mathrm{EI_y}}{L}\theta_{22\mathrm{y}} + \frac{24\mathrm{EI_y}}{L^2}\delta_\mathrm{z} - \frac{LP}{60}\theta_{21\mathrm{y}} + \frac{LP}{15}\theta_{22}\mathrm{y} + \frac{P}{10}\delta_\mathrm{z} - \frac{P}{6}\mathrm{v_{m0y}} \tag{16}$$

$$M_{22z} = \frac{4EI_z}{L}\theta_{21z} + \frac{8EI_z}{L}\theta_{22z} + \frac{24EI_z}{L^2}\delta_y - \frac{LP}{60}\theta_{21z} + \frac{LP}{15}\theta_{22z} + \frac{P}{10}\delta_y - \frac{P}{6}v_{m0z} \quad (17)$$

$$M_t = \frac{GJ}{L}\theta_x \quad (18)$$

To predict incremental displacements due to applied incremental forces, the tangent stiffness is required and calculated as follows:

$$\delta^2\Pi = \frac{\partial^2\Pi}{\partial u_i \partial u_j}\delta u_i \delta u_j = [\frac{\partial F_i}{\partial u_j} + \frac{\partial F_i}{\partial q}\frac{\partial q}{\partial u_j}]\delta u_i \delta u_j \quad (19)$$

Therefore, the tangent stiffness matrix is output and written in terms of three parts as,

$$[k]_e = [k]_L + [k]_G + [k]_S \quad (20)$$

where, $[k]_e$ is the element tangent stiffness; $[k]_L$ is the linear stiffness matrix of an element; $[k]_G$ is the geometric stiffness matrix of an element; and $[k]_S$ is the spring stiffness for the internal plastic hinge.

The element stiffness matrix is to be condensed to six degrees of freedom for compatibility to the existing computer program as well as improving the numerical efficiency. The relations between the condensed stiffness matrix [k*] and the generalized force {f} are given as,

$$\{f\} = [k^*]\{u\}_e \quad (21)$$

and,

$$[k^*] = [k]_{ee} - [k]_{ie}^T[k]_{ii}^{-1}[k]_{ie} \qquad \{f\} = \{F\}_e - [k]_{ie}^T[k]_{ii}^{-1}\{F\}_i \quad (22)$$

also, the internal DOFs can be computed as,

$$\{u\}_i = [k]_{ii}^{-1}(\{F\}_i - [k]_{ie}\{u\}_e) \quad (23)$$

where, $\{u\}_e$ is the external DOFs and expressed as $\{e\ \ \theta_{11y}\ \ \theta_{11z}\ \ \theta_x\ \ \theta_{22y}\ \ \theta_{22z}\}^T$; $\{u\}_i$ is the internal DOFs as $\{\theta_{12y}\ \ \theta_{12z}\ \ \delta_z\ \ \delta_y\ \ \theta_{21y}\ \ \theta_{21z}\}^T$; $\{F\}_e$ is the force vector applied at external nodes as $\{P\ \ M_{11y}\ \ M_{11z}\ \ M_x\ \ M_{22y}\ \ M_{22z}\}^T$; and $\{F\}_i$ is the internal force vector written as $\{M_{12y}\ \ M_{12z}\ \ F_z\ \ F_y\ \ M_{21y}\ \ M_{21z}\}^T$.

2.3 Plastic Fiber Hinge Model

The degradation in hinge stiffness reflects the material yielding on hinge sections. In the plastic fiber hinge model [24], the formulations for calculating the spring stiffness S, are written as,

$$S = 10^{+10} \frac{EI_0}{L}, \text{ for } M_i^{\zeta} \le M_{er}^{\zeta} \tag{24}$$

$$S = \frac{EI(\zeta)}{L} \left| \left(M_{pr}^{\zeta} - M_i^{\zeta} \right) / \left(M_i^{\zeta} - M_{er}^{\zeta} \right) \right| \text{ for } M_{er}^{\zeta} < M_i^{\zeta} < M_{pr}^{\zeta} \tag{25}$$

$$S = \frac{EI(\zeta)}{L} \rho, \text{ for } M_i^{\zeta} \le M_{er}^{\zeta} \tag{26}$$

where EI(ζ)/L is the flexural stiffness in the current iteration; and M_{er}^{ζ} and M_{pr}^{ζ} are the elastic and plastic moments under the current axial force.

The concrete cracking of the critical section on the hinge locations are considered by an approximate method using the effective second moment of inertia, which can be calculated by the formula by Branson [33], as follows.

$$I_e = \left(M_{cr} / M_a \right)^3 I_{un} + \left[1 - \left(M_{cr} / M_a \right)^3 \right] I_{cr}, \text{ when } M_a \ge M_{cr} \tag{27}$$

$$I_e = I_{un}, \text{ when } M_a < M_{cr} \tag{28}$$

Where, M_{cr} is the cracking moment, equal to the intersected points by the combined loads and the concrete fracture surfaces; and I_{cr} represents the initial second moment of area at zero axial load without concrete tensile strength.

2.4 Cross section analysis approach

In the analysis of the HCFT composite sections, the reference axes for outputting the resultant forces are taken as the geometric centroid, and the coordinates are given as,

$$Z_{gc} = \frac{A_c Z_c + A_s Z_s}{A_c + A_s} \qquad Y_{gc} = \frac{A_c Y_c + A_s Y_s}{A_c + A_s} \tag{29}$$

where, A_s and A_c represent the area of the steel tube and concrete core respectively; Z_c, Y_c, Z_s and Y_s, denote the coordinates of the component centroid; and Z_{gc} and Y_{gc} are the calculated coordinates of the geometric centroid.

Three types of coordinate systems, namely as ZCY, zoy and uov systems, are adopted in the analysis. The ZCY axes are used for section modelling and give the global coordinates to the component centroids. The zoy and uov axes share the same origin equal to the sectional geometric centroid, and they are used implicitly in the numerical analysis procedure. The relations between these coordinate systems can be given by,

$$z = Z - Z_{pc}, \quad y = Y - Y_{pc} \tag{30}$$

$$u = z\cos\theta_n + y\sin\theta_n, \quad v = y\cos\theta_n - z\sin\theta_n \tag{31}$$

As to compute the stress resultant of the concrete core, the whole component will be divided into adequate numbers of parallel layers as illustrated in **Fig. 13** and the formulae are given as,

$$N_{xc} = \sum_{i=1}^{n_L} N_{xci}^{L} = \sum_{i=1}^{n_L}\sum_{j=1}^{n_v(i)} \int_{u_j^i}^{u_{j+1}^i} \int_0^{\bar{v}(n)} \sigma_c^i \, du d\bar{v} \tag{32}$$

$$M_{uc} = \rho \sum_{i=1}^{n_L} M_{uci}^{L} = \rho \sum_{i=1}^{n_L}\sum_{j=1}^{n_v(i)} \int_{u_j^i}^{u_{j+1}^i} \int_0^{\bar{v}(n)} [-\sigma_c^i(\bar{v} + v_n)] du d\bar{v} \tag{33}$$

$$M_{vc} = \rho \sum_{i=1}^{n_L} M_{vci}^{L} = \rho \sum_{i=1}^{n_L}\sum_{j=1}^{n_v(i)} \int_{u_j^i}^{u_{j+1}^i} \int_0^{\bar{v}(n)} \sigma_c^i u \, du d\bar{v} \tag{34}$$

where n_L represents layer number and $n_v(i)$ stands for the number of the intersected points within the layers.

The steel tube is automatically meshed into small fibres, and its stress resultant can be computed as,

$$N_{xs} = \sum_{k=1}^{n_s} \sigma_{sk} A_{sk} \qquad M_{us} = -\sum_{k=1}^{n_s} \sigma_{sk} A_{sk} v_{sk} \qquad M_{vs} = \sum_{k=1}^{n_s} \sigma_{sk} A_{sk} u_{sk} \tag{35}$$

in which, A_{sk} is the area of steel fibers; and σ_{sk} is the stress in the fiber.

The internal forces in terms of axial load and bending moments can be computed by summing up the stress resultant of the steel tube and the concrete core. Since the forces are obtained by referring to the local axes, a transformation of the bending moments from uov to zoy axes is required and given by,

$$N_x = N_{xc} + N_{xs} \tag{36}$$

$$M_u = M_{uc} + M_{us},\ M_v = M_{vc} + M_{vs} \tag{37}$$

$$M_z = M_u \cos\theta_n - M_v \sin\theta_n, M_y = M_u \sin\theta_n + M_v \cos\theta_n \tag{38}$$

Once the neutral axis of a cross section is determined, the sectional capacity can be computed. To this, the Quasi-Newton iterative strategy is adopted for calculating the height of the neutral axis d_n related to the axial force N_x, and expressed as,

$$d_{n,k} = d_n + \frac{d_n^{'} - d_n}{N_x^{'} - N_x}(N_{xd} - N_x) \tag{39}$$

in which, $d_{n,k}$ is the height of the neutral axis in the current step; d_n and d_n' denote the smaller and larger value of the height of the neutral axis in the last step; and N_x and N_x' are the corresponding axial forces with reference to the height of the neutral axis.

The sectional yield surfaces can be generated by rotating the orientation θ_n of neutral axis from 0^o to 360^o, and the overall analysis procedure for generating the sectional yield surfaces is illustrated in **Fig. 14**.

3. Constitutive Models of Confined High-strength Concrete

An accurate numerical method for direct analysis is established on the basis of the material constitutive models that fundamentally affect the simulation of CFT columns. High strength concrete is an extremely brittle material, with strength that abruptly demises once collapse occurs. When the concrete is confined by steel tubes, its ductility significantly improves as reported by Knowles and Park [1]. Hence, confinement effects must be considered in the analysis.

3.1 Stress–strain Relationship

The complete stress–strain relationship of concrete is plotted in **Fig. 6**, in which the compressive component of the constitutive relationship of concrete is taken from Eurocode 2 [31] and can be expressed as,

$$\sigma_c = f_c\left[1-\left(1-\varepsilon_c/\varepsilon_0\right)^n\right] \quad \text{when} \quad 0 \le \varepsilon_c \le \varepsilon_0 \tag{40}$$

$$\sigma_c = f_c \quad \text{when} \quad \varepsilon_{c0} \le \varepsilon_c \le \varepsilon_{cu} \tag{41}$$

in which f_c denotes for the peak design strength of concrete under compression and ranges from 12MPa to 90MPa; ε_0 and ε_{cu} are the strains at reaching the maximum strength and the ultimate, respectively. For the high-strength concrete, ε_0 equals to ε_{cu}; n represents the exponent that can be conventionally taken as 2.0 and 1.4 for normal and high strength concrete, respectively.

The confinement effect of concrete can be taken into account by modifying the stress–strain relationship indicated in the equation (1) and (2) thus:

$$f_{c,c} = f_c(1.000 + 5.0\sigma_2 / f_{ck}) \quad \text{for} \quad \sigma_2 \le 0.05 f_c \tag{42}$$

$$f_{c,c} = f_c(1.125 + 2.50\sigma_2 / f_c) \quad \text{for} \quad \sigma_2 > 0.05 f_c \tag{43}$$

$$\varepsilon_{c0,c} = \varepsilon_{c0}(f_{c,c} / f_c)^2 \tag{44}$$

$$\varepsilon_{cu,c} = \varepsilon_{cu} + 0.2\sigma_2 / f_c \tag{45}$$

in which σ_2 is the effective confining force; $f_{c,c}$ is the peak compressive strength of confined concrete; and $\varepsilon_{0,c}$ and $\varepsilon_{cu,c}$ represent the confined concrete strains at the maximum and ultimate strengths, respectively. The effective lateral confining stress for the circular and octagonal tubular sections are discussed in the next section.

The strain softening model proposed by Bazant [34] is adopted as the tensile part of the constitutive relationship of concrete. It is described as follows:

$$\sigma_c = -E_c \varepsilon_c \quad \text{for} \quad \varepsilon_{t0} \le \varepsilon_c \le 0 \tag{46}$$

$$\sigma_c = -\left[f_t - (\varepsilon_c - \varepsilon_{t0}) E_t \right] \quad \text{for} \quad \varepsilon_{tu} \le \varepsilon_c \le \varepsilon_{t0} \tag{47}$$

$$E_t = 70 E_c / (57 + 145 f_t) \tag{48}$$

where σ_c is the stress of concrete at specific strain ε_c; E_c and E_t are the modulus of elasticity and tangent tensile strain softening modulus, respectively; and ε_{t0} and ε_{tu} denote the strains at peak tensile strength and tensile fracture, respectively.

3.2 Confinement action in circular CFT sections

The lateral pressure σ_2 is a vital factor that determines the confinement action on the concrete in a steel tube. In circular CFT sections, this confining stress σ_{2o} can be calculated from the force-equilibrium condition, indicated in **Fig. 7** (a), and given as:

$$\sigma_{2c}(D - 2t) = 2\sigma_\theta t \tag{49}$$

And it can be rewritten as:

$$\sigma_{2c} = \frac{2t}{D - 2t}\sigma_\theta = \frac{2}{D/t - 2}\sigma_\theta \tag{50}$$

in which, σ_{2c} is the effective confining stress for the confined concrete in the circular tubular section; D and t are the diameter and plate thickness of the circular tube, respectively; and σ_θ is the hooping stress of the steel tube.

Furthermore, a factor k for reflecting the effectiveness of the confining action by referring to the circular tube is introduced and the equation in (50) is further revised as:

$$\sigma_2 = k\frac{2}{D/t - 2}\sigma_\theta \tag{51}$$

where, k is the factor for evaluating the effective confining stress, and it is empirically assumed as 0.85 for high-strength concrete.

The D/t ratio in equations (50) and (51) is limited to a maximum value, which is defined in Eurocode 4 [35] and given as:

$$\mathrm{Max}\left(\frac{\mathrm{D}}{\mathrm{t}}\right) = 90 * \frac{235}{\mathrm{f_y}} \tag{52}$$

in which, f_y is the design strength of steel tube.

3.3 Confinement action in octagonal CFT sections

The lateral pressure acting on the confined concrete core in an octagonal CFT section is illustrated in **Fig. 7** (b). In the present study, an approximated method by assuming the effective confining zone is proposed as given in **Fig. 8**. And a reduction factor η is proposed and can be derived as:

$$\eta = \frac{\pi d^2/4}{\pi D^2/4} = \left(\frac{d}{D}\right)^2 = (\cos 22.5^0)^2 = 0.854 \tag{53}$$

By submitting the equation (52) into (51), the effective confining stress for the octagonal tubular section is given as:

$$\sigma_{2o} = k\frac{2}{D/t-2}\eta\sigma_\theta = k\frac{1.7}{D/t-2}\sigma_\theta \tag{54}$$

4. Experimental Investigation

The experimental investigation aimed to study the material characteristics of HSC confined in circular and octagonal steel tubes. A series of uni-axial and tri-axial compression tests on HSC specimens was designed. The specimens discussed in the preceding section are shown in **Fig. 15**. For comparison, a group of unconfined specimens are tested (**Fig. 16**). The dimensions of the two groups of confined specimens, namely CHS 194 and OHS 194, are presented in Table 1 and Table 2, respectively.

4.1 High strength concrete properties

Standard tests for cube and cylinder concrete specimens were conducted in accordance with Eurocode 2 [31] to evaluate the fundamental material characteristics of the HSC. The dimensions of the specimens are 100 × 100 × 100 mm and 150 mm diameter × 300 mm height for cube and cylinder specimens respectively. Strain gauges with 120 mm in length

were used to measure the vertical strain of the concrete specimens. The concrete cubes and cylinders were then crushed to failure to determine the compressive strength using the-house compression machines at the loading rates of 2 kN/second and 0.13 mm/min respectively.

To obtain the material characteristics of concrete, the cube and cylinder tests had been conducted at 28 days, 32 days and 50 days, and the results are tabulated in Table 3. From the results, it can be seen that, the compressive strength was still increasing after 28 days. However, a more objective comparison can be made by testing the unconfined specimens with the same size of the concrete core in confined specimens. The comparisons will be presented in the following sections.

4.2 Experimental Design

The experimental program aimed to investigate the material characteristics of HSC confined in steel tubes. Thus, vertical load is applied only on the concrete core. To facilitate the alignment of vertical load and to avoid the direct exertion of stress on the steel tubes, a 32-mm thick loading pad was placed on top of the specimens, which were slightly smaller than the concrete core (**Fig. 17**).

Theoretically, the confinement effect does not exist at the early stage of loading owing to the fact that the Poisson's ratio of concrete (typically 0.2 for uncracked concrete, Eurocode-2 [31]) is lower than that of steel (typically 0.3, Eurocode-3 [36]) at the initial loading stage. The concrete core of the specimen is then loaded axially, generating Poisson-type lateral expansion that reacts with the steel tube to develop confinement, which is also called as passive confinement. However, as the axial load increases, the lateral expansion of concrete gradually becomes greater than the steel due to the change in the Poisson's ratio of concrete, and hence a radial pressure is developed at the concrete–steel interface. At this stage, confinement of the concrete core is achieved and the steel is in hoop tension.

Although the vertical load is only applied on concrete core, the vertical shear force caused by friction is transferred across the steel tube to the concrete core interface. Besides the hoop stress is induced by the concrete expansion, the stress state can then be determined by the Von-Mises yield criterion as illustrated below:

$$\sigma_s = \sqrt{\sigma_v^2 + \sigma_\theta^2 - \sigma_v \sigma_\theta} \tag{55}$$

in which, σ_s is the current Von-Mises stress in the steel tube; σ_v is the stress at the vertical direction; and σ_θ denotes for the hooping stress in the tube.

Strain gauges were attached on the outer surface of the steel tubes to evaluate the actual stress. Strain gauges were also used to measure the hoop and axial strains of the outer surface of the steel tube at two diametrically opposite points at the mid height of each specimen. The specimen setup is shown in **Fig. 18**. The vertical strain on the concrete core was measured by the direct deformation measurements using linear variable displacement transducers (LVDTs). The experimental setup is shown in **Fig. 19**.

4.3 Material characteristics of steel tube

The material properties of the steel tubes were determined by conducting tension tests on tensile coupons, which were machined from the walls of the tubes from the two specimen groups (i.e., CHS 194 and OHS 194). The specimens were prepared according to BS EN 10002 [37], and four specimens were tested at each group. Standard experimental procedure was followed with the loading rate as 0.002 mm/minute. The results are summarized in Table 4.

4.4 Experimental results

The axial stress–strain relationships of the confined concrete core are illustrated in **Fig. 20**. The effects of confinement are highly apparent both as the axial strength and ductility of the specimens increase. As previously mentioned, another comparison groups with the

unconfined specimens are also tested. The experimental results for the CHS 194 group and OHS 194 group specimens are plotted in **Fig. 21** and **Fig. 22**, respectively.

The results for the two groups are shown in Table 5. Some of the experimental findings are discussed as follows. (1) Although HSC is brittle, its ductility in the circular and octagonal tubes significantly increases. (2) The strength enhancement of HSC is also observed in the two comparison groups, in which ultimate compressive strength increases to 69% and 45% in the circular and octagonal groups, respectively. (3) An apparent confinement effect is observed in the core of the octagonal tubes. The hooping stresses of the steel tubes were measured in the experiment. By using the equation (51) and equation (53) proposed for the circular and octagonal tubular sections, respectively, the effective confining stress can be determined. Consequentially, the material constitutive model of confined concrete can be generated. Comparison results with the experiment and the present models are tabulated in Table 6. The present study showed satisfactory in predicting the ultimate strength of confined HSC in the circular and octagonal tubes.

5. Verification Examples

To verify the accuracy, efficiency and versatility of the present method for the proposed design approach, several examples are selected and presented as following.

5.1 Analysis of high-strength concrete-filled circular and octagonal sections

In this example, two high-strength-concrete-filled tubular sections with circular and octagonal shapes are analyzed. Same section dimensions are assumed for the two sections, and the diameters and plate thickness are 500mm and 25mm, respectively. The steel grade is S355, where the design tensile strength f_y, shear strength f_{yv} and Young's modulus are 355MPa, 204.96MPa and 205GPa, respectively. High-strength concrete is adopted for the two HCFT sections, where the concrete grade is C80/95 and the other parameters as design

strength f_{cd}, initial yield strain ε_0 and fracture strain ε_c are 53.33MPa, 0.0025 and 0.0026, respectively.

The effective confining stresses for the circular and octagonal sections are 19.36 MPa and 16.45MPa, respectively. The comparisons for the plain and confined high-strength concrete are plotted in the **Fig. 23**. From the comparison, it clearly indicates the consideration of the confinement effects can dramatically increase the sectional capacities in terms of compressive and flexural strengths.

5.2 Experimental verification with the circular HCFT columns

The experimental investigations on high-strength-concrete-filled circular hollow steel columns conducted and reported by Neogi and Sen [38] are referenced for verifying the proposed numerical method. Ten columns are analyzed with both ends pinned and modeled by one element per member. To confirm the versatility, the recoded deflection under loads of the column M5 is compared with the predicted results by the current approach shown in **Fig. 25**, where indicates slight difference between two curves by the present theory and by experiment. It further indicates the versatility of the proposed plastic analysis method for design and analysis of the CFT columns. The analysis results for the other columns are given from **Fig. 26** to **Fig. 28**, and also summarized in Table 7 which indicates the claim of the proposed theory being accurate and efficient.

6. Conclusions

This paper proposes a numerical-based design method for direct analysis of HCFT columns with circular and octagonal sections, considering imperfections, large deflection, material yielding and concrete cracking effects. In contract to hot-rolled circular hollow sections of size commonly limited to 500mm, the polygonal structural form has virtually no limitation in its size so its application as mega columns in high-rise buildings is practically attractive with confinement effects considered. To simulate the behaviors of the HCFT columns, a curved-

piecewise-Hermite (CPH) element is proposed in this paper. A plastic fiber hinge model using the sectional yield surfaces is introduced for reflecting yielding behavior at hinge locations. The sectional yield surfaces for HCFT sections are generated by a robust cross-sectional analysis technique elaborated in this paper. The material constitutive models for the confined high-strength concrete in steel tubes are investigated by an experiment. The lateral pressure exerted on the concrete core in a circular tubular section can be calculated by the force-equilibrium. The effective confining stress for the concrete in the octagonal tube has been proposed based on the effective confinement area and the corresponding strain vs. stain curves are determined. Experimental results showed that, the strength of HSC increased dramatically increased in two groups, and the ductility was significantly improved. The present study showed satisfactory in predicting the material behaviors of confined HSC. The distinct feature of this research includes the integration of the high-performance element with the rigorous section analysis technique, which only requires the basic material properties. Finally, several examples are conducted to verify the accuracy, efficiency and effectiveness of the proposed semi-analytical and computational model.

Acknowledgements

The authors would like to express their gratitude towards the specimens provided by the Gammon Construction Limited and the technical support from the Structural Engineering Research Laboratory at the Hong Kong Polytechnic University. The authors are grateful to the financial supports by the Research Grant Council of the Hong Kong SAR Government on the project “Second-order and Advanced Analysis of Arches and Curved Structures (PolyU 152012/14E)” and by the Innovative Technology Fund for the project “Advanced design of flexible barrier systems by large deflection theory (ITS/032/14)”. The financial support from the Hong Kong Polytechnic University (PolyU: G-UC75) is also gratefully acknowledged. This publication was also partly supported by the research funding from the Construction

Industry Council under the project “Application of Polygonal High Strength Concrete-filled Composite Column in Seismic-resistant Buildings in Hong Kong” and the Hong Kong Branch of Chinese National Engineering Research Centre for Steel Construction supported by The Innovation and Technology Fund of the Hong Kong SAR Government for the project "Advanced Numerical Analyses for Building Structures Using High Performance Steel Materials". The first author further appreciates the financial support by the Faculty of Construction and Environment through the project "FCE Postdoctoral Fellow Scheme".

References

[1] R.B. Knowles, R. Park, Strength of concrete filled steel columns, Journal of the structural division, (1969).

[2] J. Wardenier, J.A. Packer, X.-L. Zhao, G.J. van der Vegte, Hollow sections in structural applications, Bouwen met Staal Rotterdam,, The Netherlands, 2010.

[3] L.H. Han, W. Li, R. Bjorhovde, Developments and advanced applications of concrete-filled steel tubular (CFST) structures: Members, Journal of Constructional Steel Research, 100 (2014) 211-228.

[4] M. Tomii, K. Yoshimura, Y. Morishita, Experimental studies on concrete-filled steel tubular stub columns under concentric loading, in: Stability of Structures Under Static and Dynamic Loads, ASCE, 1977, pp. 718-741.

[5] K. Tanaka, Y. Kanoh, M. Teraoka, A. Sasaki, Axial compressive behaviour of composite short column using high strength concrete, Proc Jap Concrete Inst, 12 (1990) 83-88.

[6] S. Schneider, Axially Loaded Concrete-Filled Steel Tubes, Journal of Structural Engineering, 124 (1998) 1125-1138.

[7] C. Huang, Y. Yeh, G. Liu, H. Hu, K. Tsai, Y. Weng, S. Wang, M. Wu, Axial Load Behavior of Stiffened Concrete-Filled Steel Columns, Journal of Structural Engineering, 128 (2002) 1222-1230.

[8] M. Mursi, B. Uy, Strength of Concrete Filled Steel Box Columns Incorporating Interaction Buckling, Journal of Structural Engineering, 129 (2003) 626-639.

[9] H. Hu, C. Huang, M. Wu, Y. Wu, Nonlinear Analysis of Axially Loaded Concrete-Filled Tube Columns with Confinement Effect, Journal of Structural Engineering, 129 (2003) 1322-1329.

[10] X. Dai, D. Lam, Numerical modelling of the axial compressive behaviour of short concrete-filled elliptical steel columns, Journal of Constructional Steel Research, 66 (2010) 931-942.

[11] T. Sheehan, X.H. Dai, T.M. Chan, D. Lam, Structural response of concrete-filled elliptical steel hollow sections under eccentric compression, Engineering Structures, 45 (2012) 314-323.

[12] E. Ellobody, Numerical modelling of fibre reinforced concrete-filled stainless steel tubular columns, Thin-Walled Structures, 63 (2013) 1-12.

[13] X.H. Dai, D. Lam, N. Jamaluddin, J. Ye, Numerical analysis of slender elliptical concrete filled columns under axial compression, Thin-Walled Structures, 77 (2014) 26-35.

[14] K. Susantha, G. Hanbin, T. Usami, A capacity prediction procedure for concrete-filled steel columns, Journal of earthquake engineering, 5 (2001) 483-520.

[15] K.A.S. Susantha, H. Ge, T. Usami, Uniaxial stress–strain relationship of concrete confined by various shaped steel tubes, Engineering Structures, 23 (2001) 1331-1347.

[16] Q.Q. Liang, S. Fragomeni, Nonlinear analysis of circular concrete-filled steel tubular short columns under eccentric loading, Journal of Constructional Steel Research, 66 (2010) 159-169.

[17] D. Candappa, J. Sanjayan, S. Setunge, Complete Triaxial Stress-Strain Curves of High-Strength Concrete, Journal of Materials in Civil Engineering, 13 (2001) 209-215.

[18] J. Y. Richard Liew, M. X. Xiong, D. X. Xiong, Design of High Strength Concrete Filled Tubular Columns For Tall, The International Journal of High-Rise Buildings, 3 (2014).

[19] S.L. Chan, Z.H. Zhou, 2nd order elastic analysis of frames using single imperfect element per member, Journal of Structural Engineering-ASCE, 121 (1995) 939-945.

[20] S.L. Chan, J.X. Gu, Exact tangent stiffness for imperfect beam-column members - Closure, Journal of Structural Engineering-ASCE, 127 (2001) 1492-1494.

[21] S.W. Liu, Y.P. Liu, S.L. Chan, Direct analysis by an arbitrarily-located-plastic-hinge element - Part 1: Planar analysis, Journal of Constructional Steel Research, 103 (2014) 303-315.

[22] S.W. Liu, Y.P. Liu, S.L. Chan, Direct analysis by an arbitrarily-located-plastic-hinge element - Part 2: Spatial analysis, Journal of Constructional Steel Research, 103 (2014) 316-326.

[23] W.F. Chen, S.L. Chan, 2nd-order inelastic analysis of steel frames using element with midspan and end springs, Journal of Structural Engineering, ASCE, 121 (1995) 530-541.

[24] T.J. Li, S.W. Liu, and S.L. Chan. Direct analysis for high-strength steel frames with explicit-model of residual stresses. Engineering Structures 100 (2015): 342-355.

[25] S.W. Liu, Y.P. Liu, S.L. Advanced analysis of hybrid steel and concrete frames: part 1: cross-section analysis technique and second-order analysis. Journal of Constructional Steel Research 70 (2012): 326-336.

[26] J. Mander, M. Priestley, R. Park, Theoretical Stress‐Strain Model for Confined Concrete, Journal of Structural Engineering, 114 (1988) 1804-1826.

[27] D. Cusson, P. Paultre, Stress-Strain Model for Confined High-Strength Concrete, Journal of Structural Engineering, 121 (1995) 468-477.

[28] B. Binici, An analytical model for stress–strain behavior of confined concrete, Engineering Structures, 27 (2005) 1040-1051.

[29] W. Lokuge, J. Sanjayan, S. Setunge, Stress–Strain Model for Laterally Confined Concrete, Journal of Materials in Civil Engineering, 17 (2005) 607-616.

[30] A.K. Samani, M.M. Attard, A stress–strain model for uniaxial and confined concrete under compression, Engineering Structures, 41 (2012) 335-349.

[31] The European Committee for Standardization (CEN), Eurocode 2: Design of Concrete Structures: Part 1-1: General Rules and Rules for Buildings, 2004.

[32] S.L. Chan, Large Deflection Kinematic Formulations for 3-Dimensional Framed Structures, Computer Methods in Applied Mechanics and Engineering, 95 (1992) 17-36.

[33] D.E. Branson, G.A. Metz, Instantaneous and time-dependent deflections of simple and continuous reinforced concrete beams, Dept. of Civil Engineering and Auburn Research Foundation, Auburn University, Auburn, Ala., 1963.

[34] Z. Bazant, J. Pan, G. Pijaudier‐Cabot, Softening in Reinforced Concrete Beams and Frames, Journal of Structural Engineering, 113 (1987) 2333-2347.

[35] The European Committee for Standardization (CEN), Eurocode 4: Design of composite steel and concrete structures: Part 1-1: General rules and rules for buildings, 2005.

[36] The European Committee for Standardization (CEN), Eurocode 3: Design of steel structures: Part 1-1: General rules and rules for buildings, 2005.

[37] British Standards Institution, BS EN 10002-1: 2001. Tensile testing of metallic materials. Method of test at ambient temperature, 2001.

[38] P.K. Neogi, H.K. Sen, Concrete-filled tubular steel columns under eccentric loading, The structural engineer, 47 (1969) 9.

Tables

Table 1. Dimensions of confined specimens in CHS 194 group

Specimen	Tube Thickness	External Diameter	Height	Concrete Area	Steel Area
	mm	mm	mm	mm^2	mm^2
C1-B	5.00	193.80	369.04	26533	2966
C1-C	4.99	193.36	368.48	26412	2953

Table 2. Dimensions of confined specimens in OHS 194 group

Specimen	Tube Thickness	Edge Length	Height	Concrete Area	Steel Area
	mm	mm	mm	mm^2	mm^2
O1-A	5.01	73.73	369.72	23376	2872
O1-B	5.00	73.81	368.30	23435	2870

Table 3. Strength of concrete obtained from cube and cylinder test

Test day	Cube Strength f_{cu}	Cylinder Strength f_c	f_{cu}/f_c
	MPa	MPa	
28 days	98	76	0.77
32 days	115		
50 days	126	96	0.76

Table 4. Steel properties obtained from coupon test

Group	f_y	f_u	E_s	ε_e	E_u	Possion's ratio
	MPa	MPa	GPa	mm/mm	GPa	
CHS-194	379	515	207	0.0170	1.24	0.3
OCT-194	290	455	202	0.0096	1.21	0.3

Table 5. Summarized experimental results

Confined shape	D/t ratio	Yield strength of steel	Unconfined concrete strength	Confined concrete strength	Concrete strength increased
		MPa	MPa	MPa	
Circular	38.75	379.25	80.85	136.62	69%
Octagonal	38.52	289.50	82.74	120.15	45%

Table 6. Comparison results with the experiment and the present models

Specimen	Shape	σ_θ	σ_2	$f_{c,c}$	$f_{exp.}$	$f_{c,c}/ f_{exp.}$
		MPa	MPa	MPa	MPa	
C1-B	Circular	378.7	17.4	134.4	134.4	1.00
C1-C	Circular	372.9	17.1	133.7	138.8	0.96
O1-A	Octagonal	299.5	11.7	122.4	122.3	1.00
O1-B	Octagonal	300.6	11.8	122.5	118.0	1.04
Mean						1.00

Table 7. Summarized comparison results of circular CFT columns

Column Mark	Experiment kN	Present Study kN	Exp./Pres.
M1	622	636	0.98
M2	702	720	0.98
M3	600	590	1.02
M4	625	609	1.03
M5	653	648	1.01
M6	739	739	1.00
M7	758	751	1.01
M8	548	577	0.95
M9	548	548	1.00
M10	417	394	1.06
Average			1.00

Figures

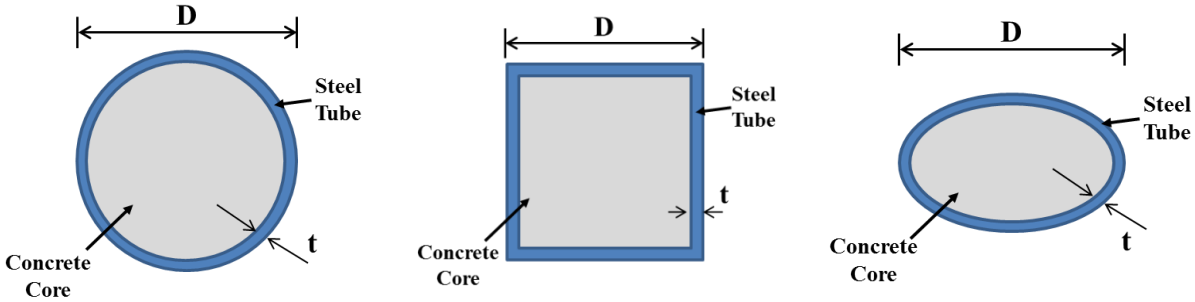

(a) Circular (b) Rectangular (c) Elliptical

Fig. 1 Typical concrete-filled-tubular (CFT) columns with normal-size sections

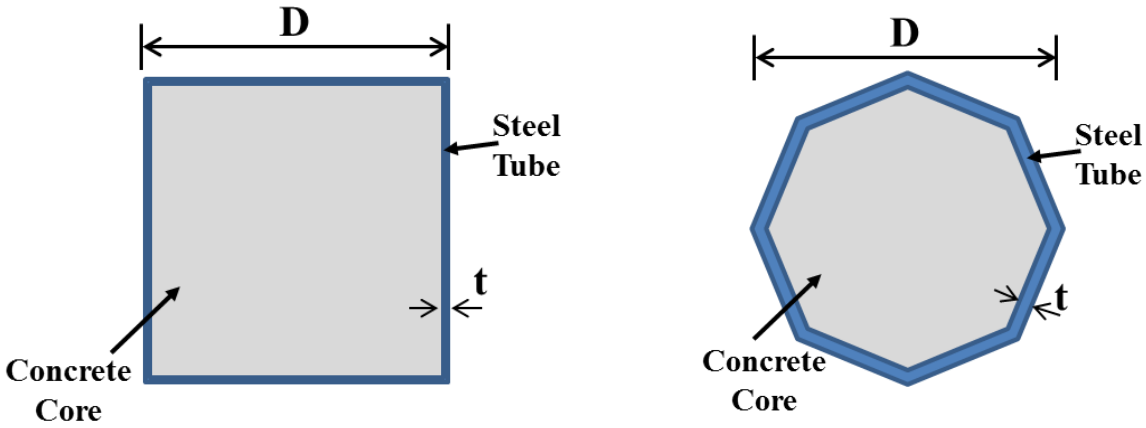

(a) Rectangular (b) Octagonal

Fig. 2 Concrete-filled-tubular (CFT) columns with large-size sections

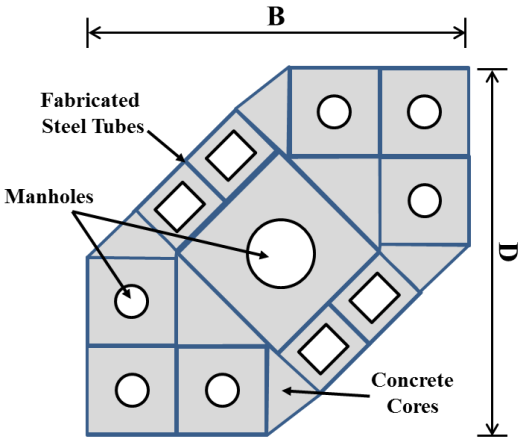

Fig. 3 Concrete-filled-tubular (CFT) columns with mega-size sections

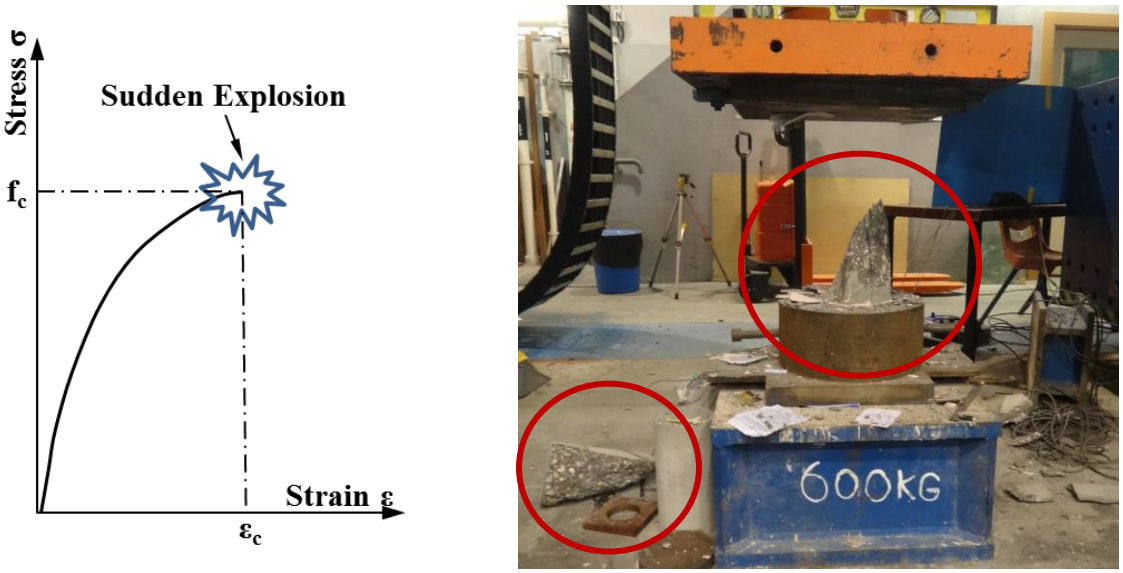

(a) Behavior of high-strength concrete (b) Exploded high-strength concrete core

Fig. 4 Failure mode of the unconfined high-strength concrete column

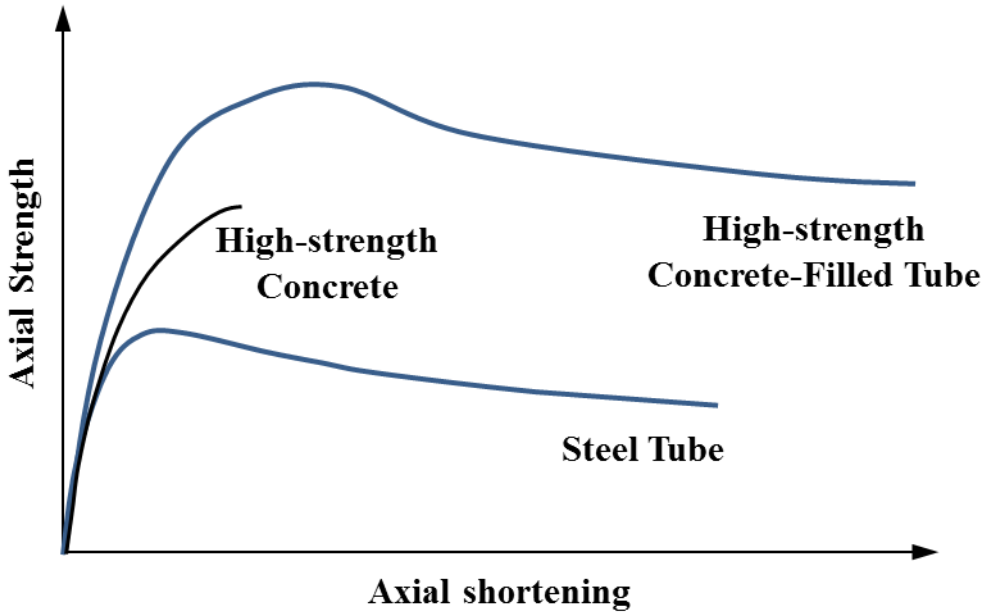

Fig. 5 Schematic compressive behavior of HCFT columns

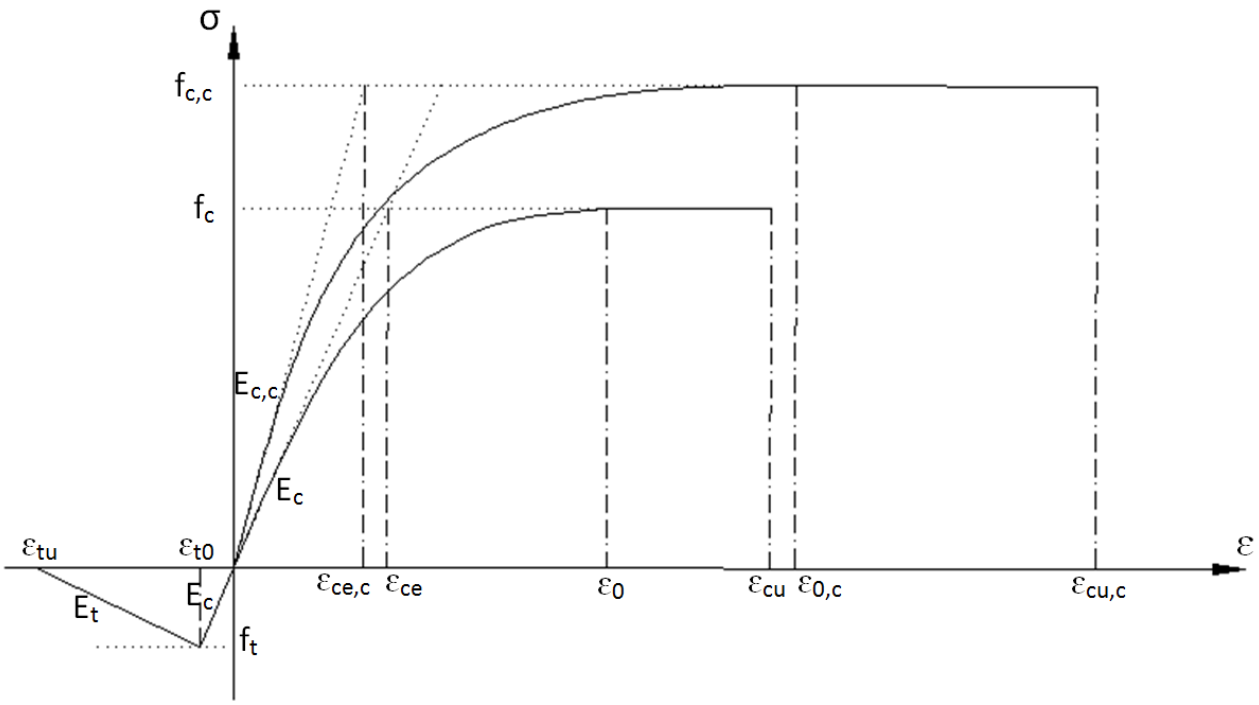

Fig. 6 Complete stress–strain relationship of confined and unconfined concrete

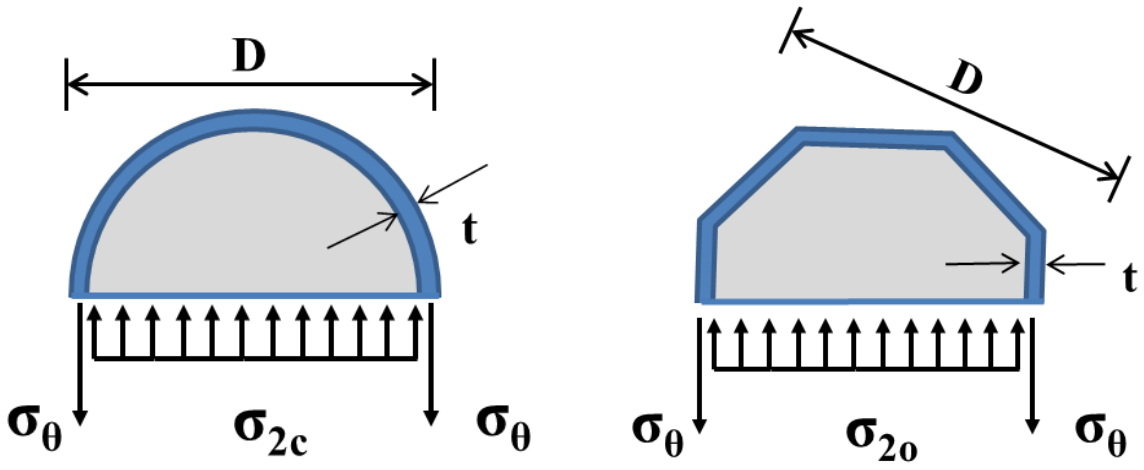

(a) Circular section (b) Octagonal section

Fig. 7 Confining pressure in circular and octagonal tubular sections

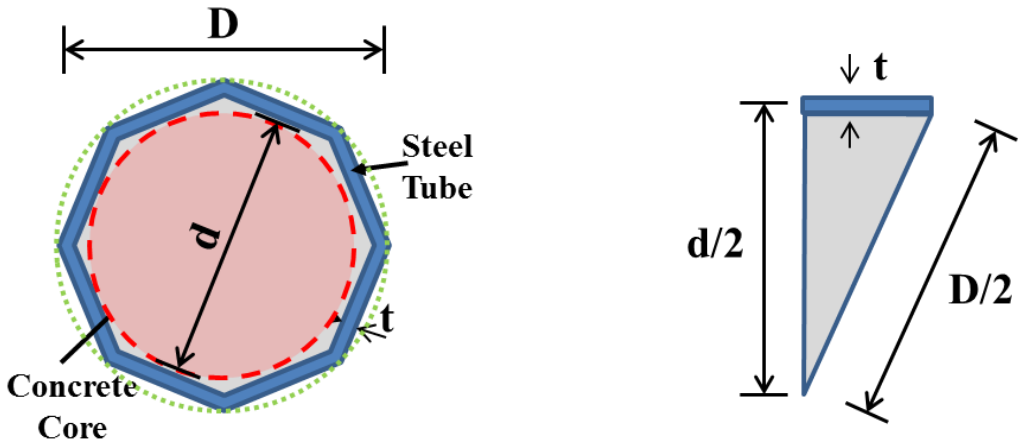

(a) Effective confinement area

(b) Relation

Fig. 8 Effective confinement area in octagonal tubular section

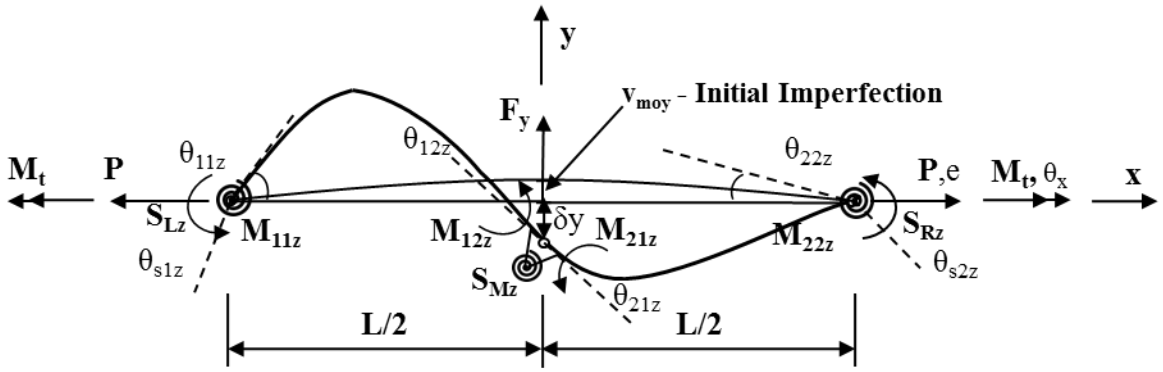

(a) Deflection along local y-axis

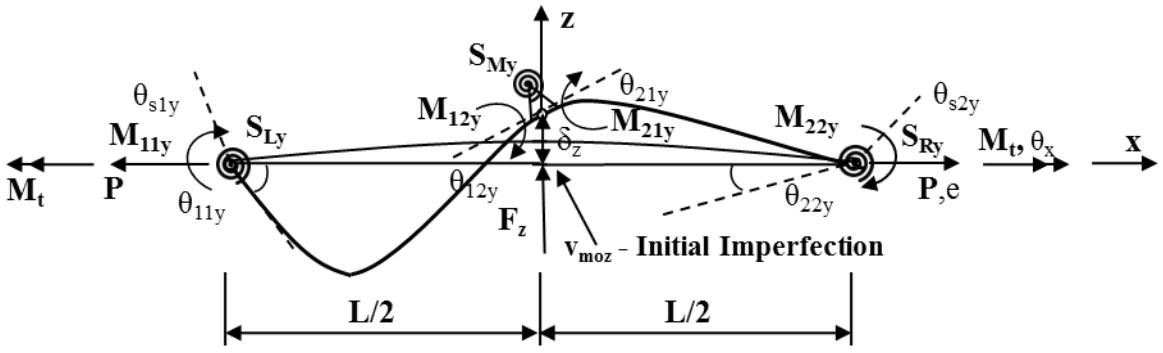

(b) Deflection along local z-axis

Fig. 9 Forces vs. deflections of curved-piecewise-Hermite (CPH) element

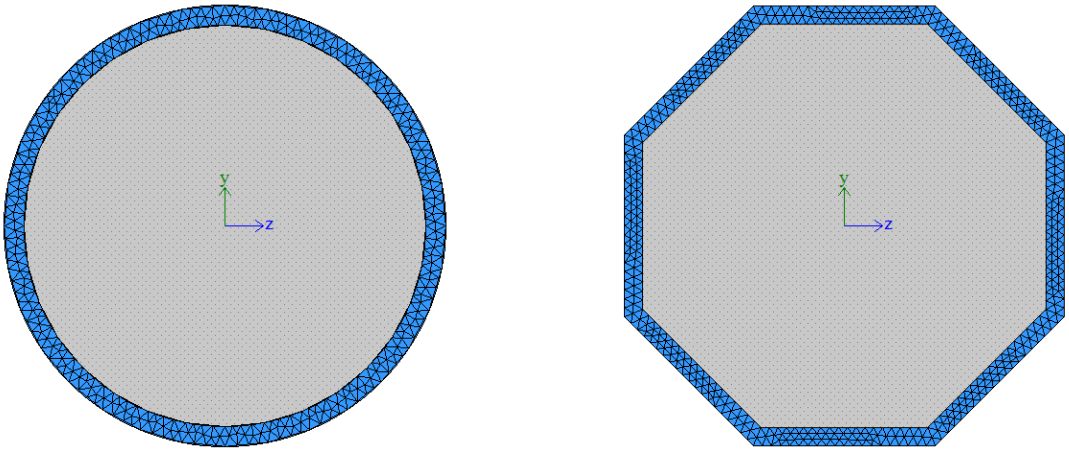

(a) Circular section (b) Octagonal section

Fig. 10 Modeling of circular and octagonal concrete-filled sections

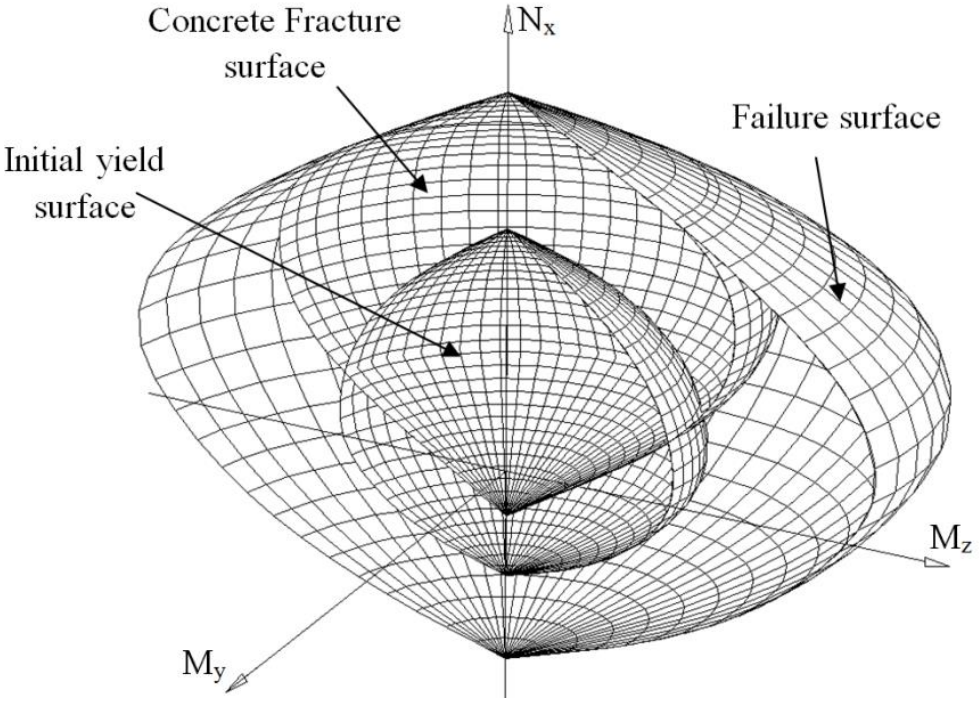

Fig. 11 Initial yield, failure, and concrete fracture surfaces of a cross section

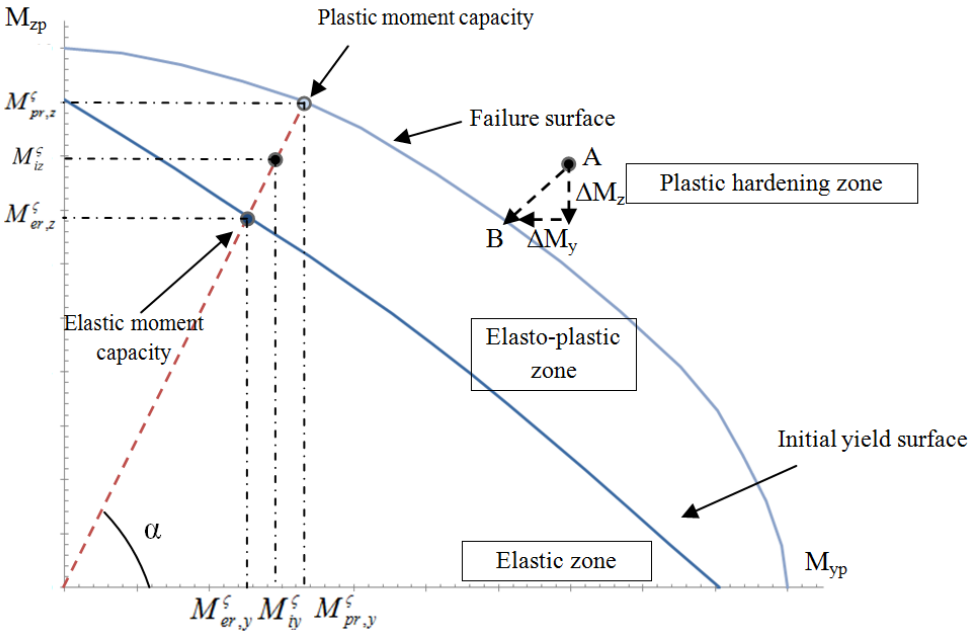

Fig. 12 Elastic and plastic moments for plastic fiber hinge model

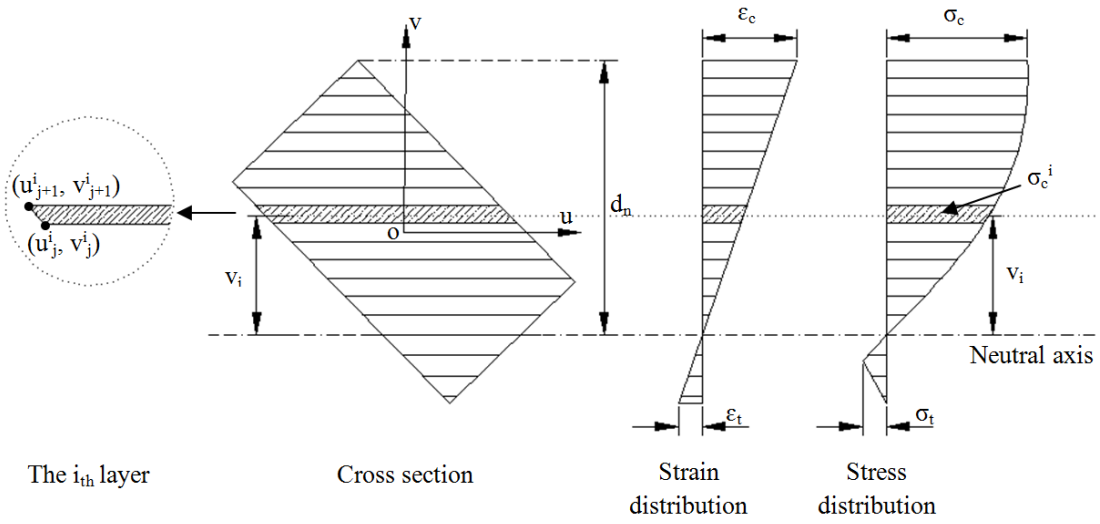

Fig. 13 Stress resultants of concrete component

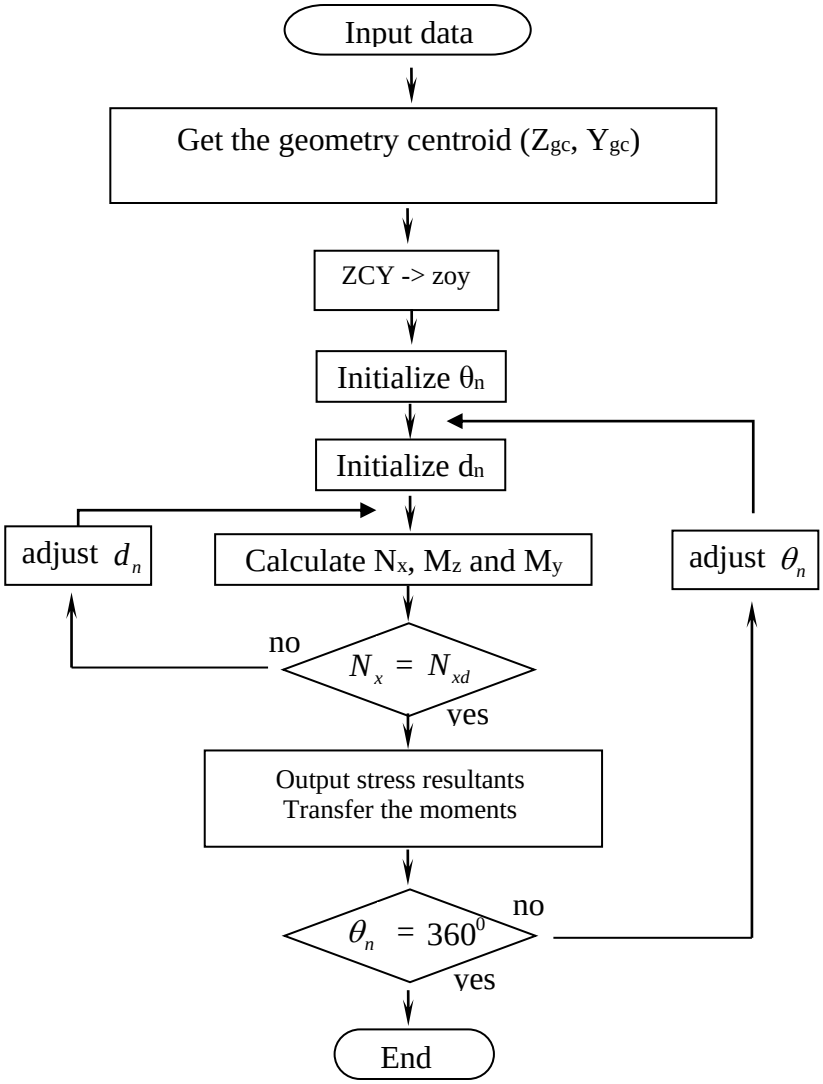

Fig. 14 Procedure for generating the sectional yield surfaces

(a) Circular confined specimen

(b) Octagonal confined specimen

Fig. 15 Confined specimens with same *D*/*t* ratio

(a) Circular unconfined specimen

(b) Octagonal unconfined specimen

Fig. 16 Unconfined specimens with the same size of concrete core

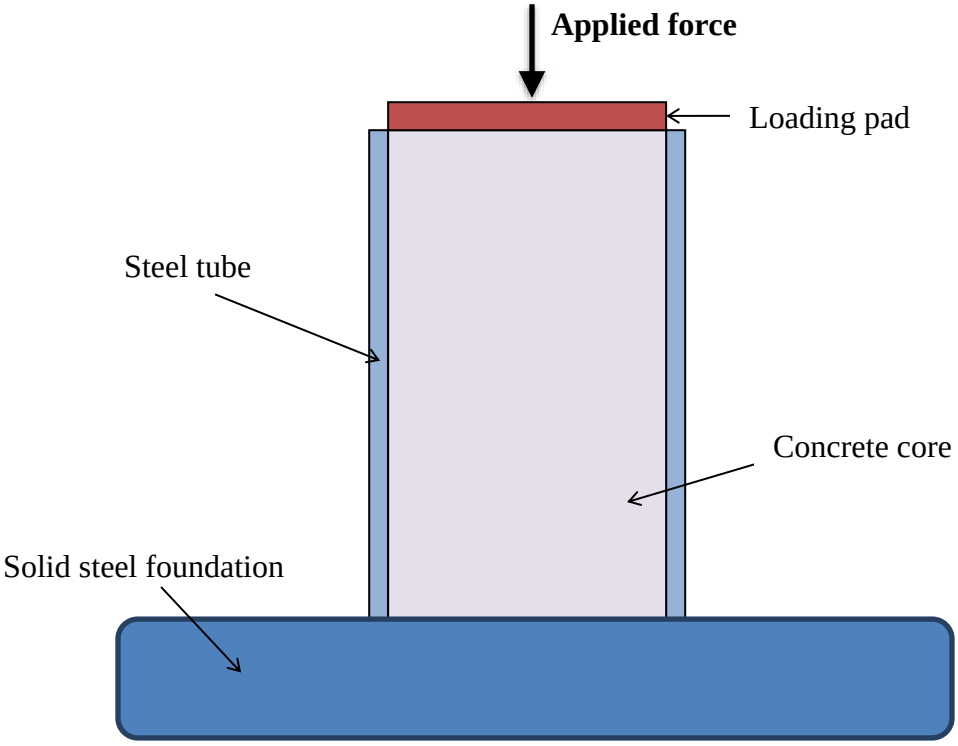

Fig. 17 Schematic test setup

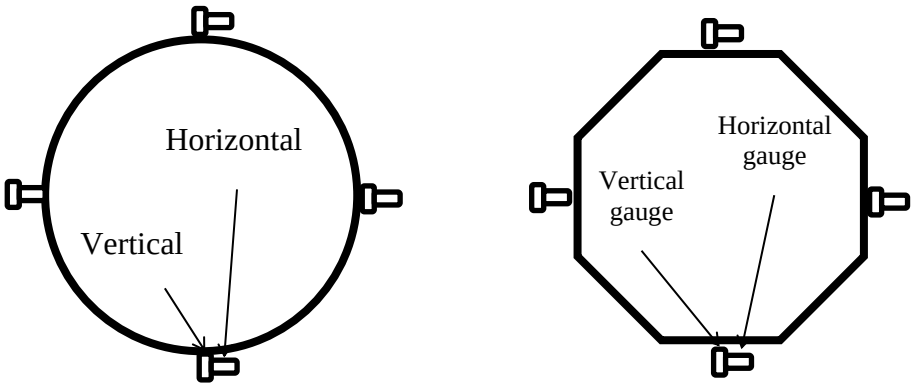

(a) Circular tube (b) Octagonal tube

Fig. 18 Strain gauges setup for confined specimens

(a) Circular confined specimens

(b) Octagonal confined specimens

Fig. 19 Experimental setup for confined specimens

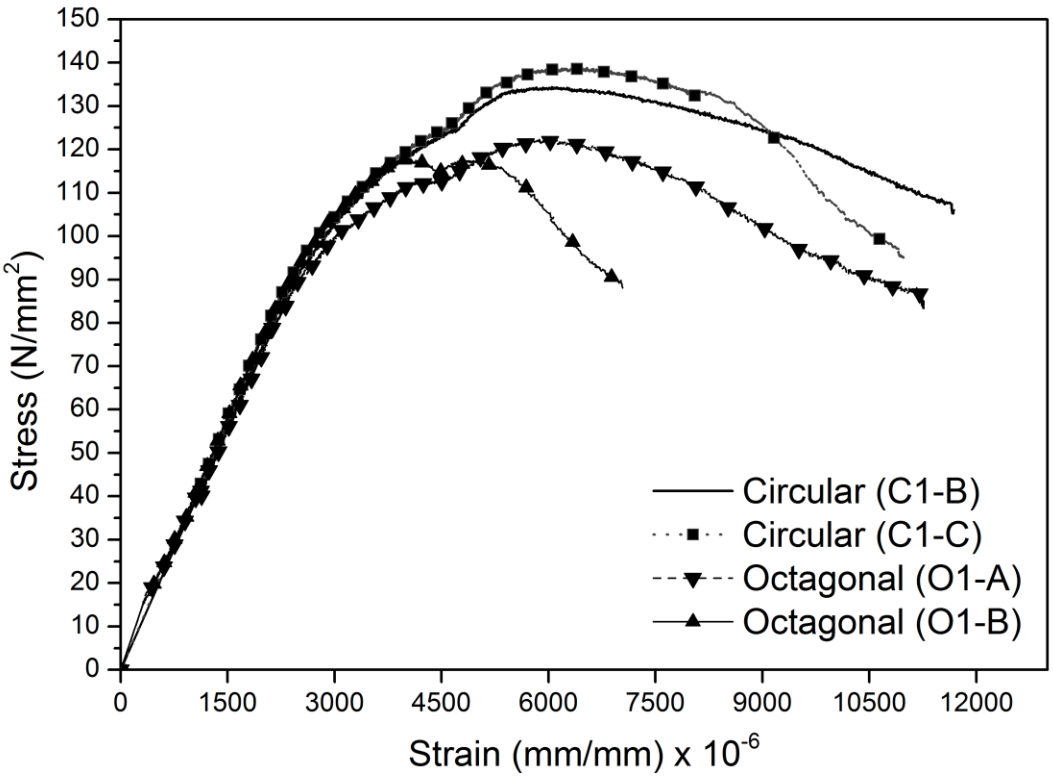

Fig. 20 Stress-strain curves of confined specimens

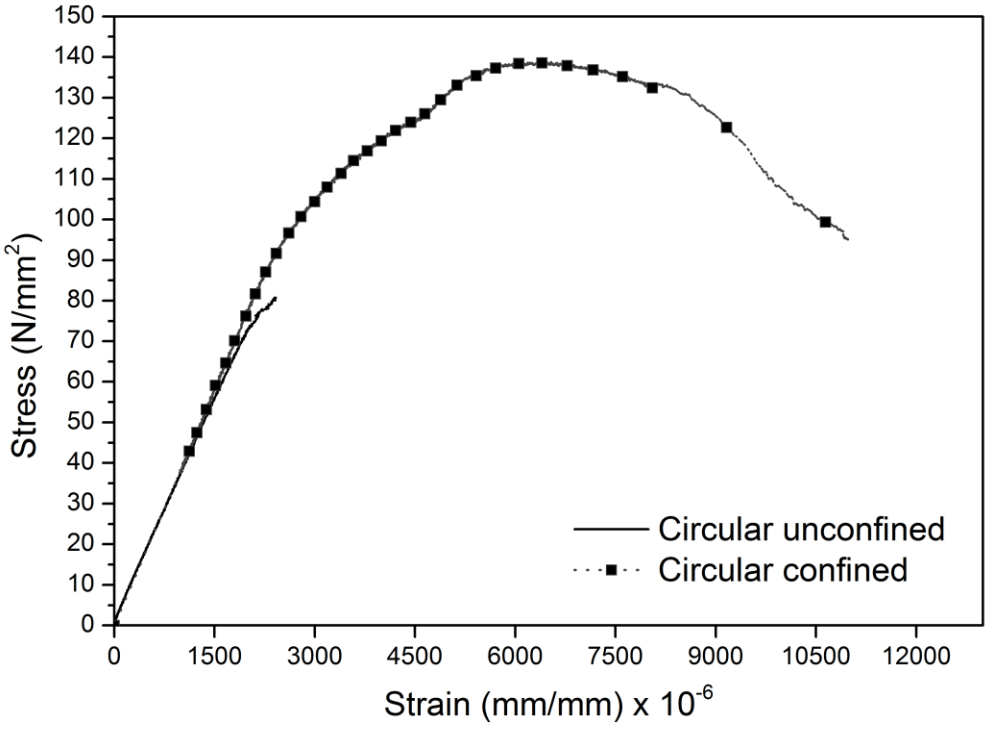

Fig. 21 The results between the circular confined and unconfined specimens

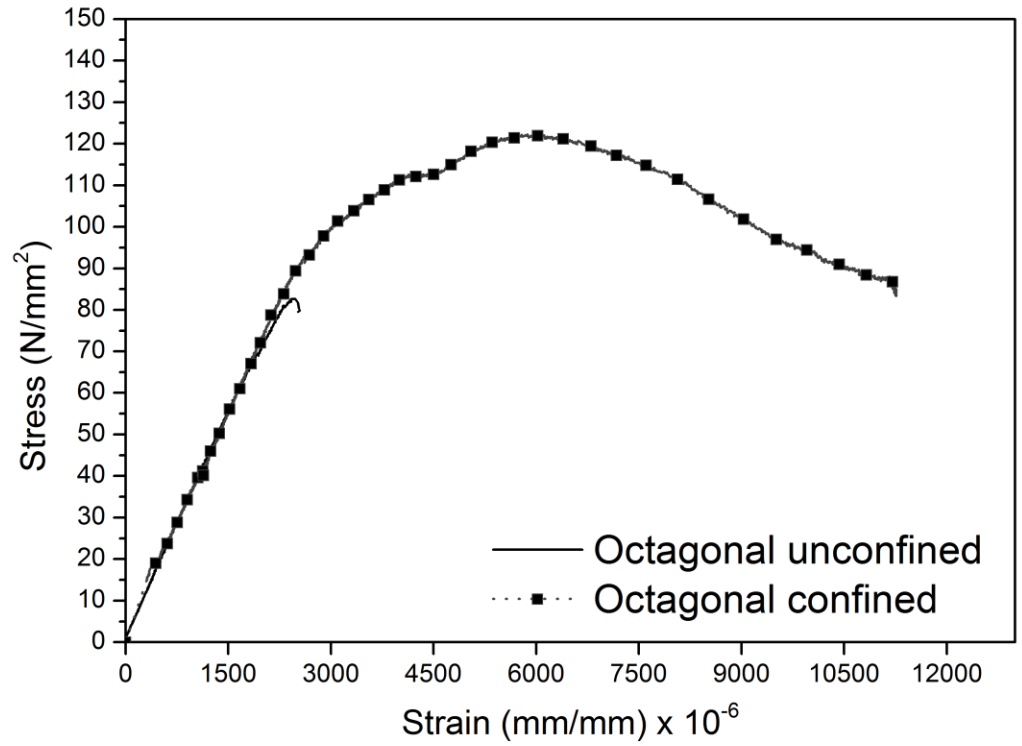

Fig. 22 The results between the octagonal confined and unconfined specimens

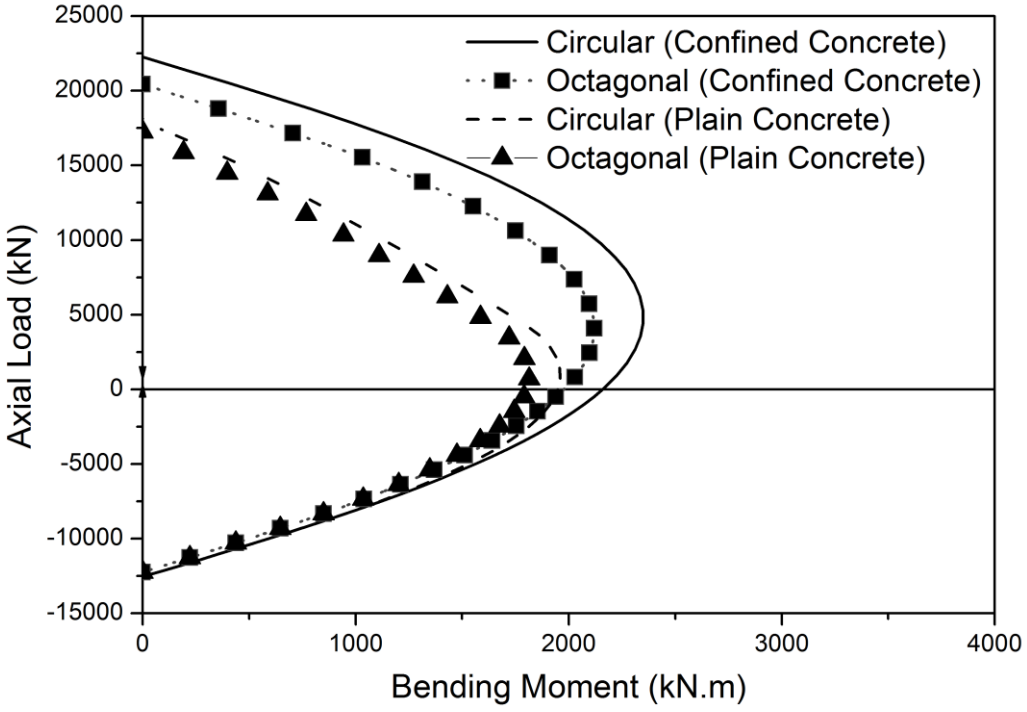

Fig. 23 P-M interaction curves

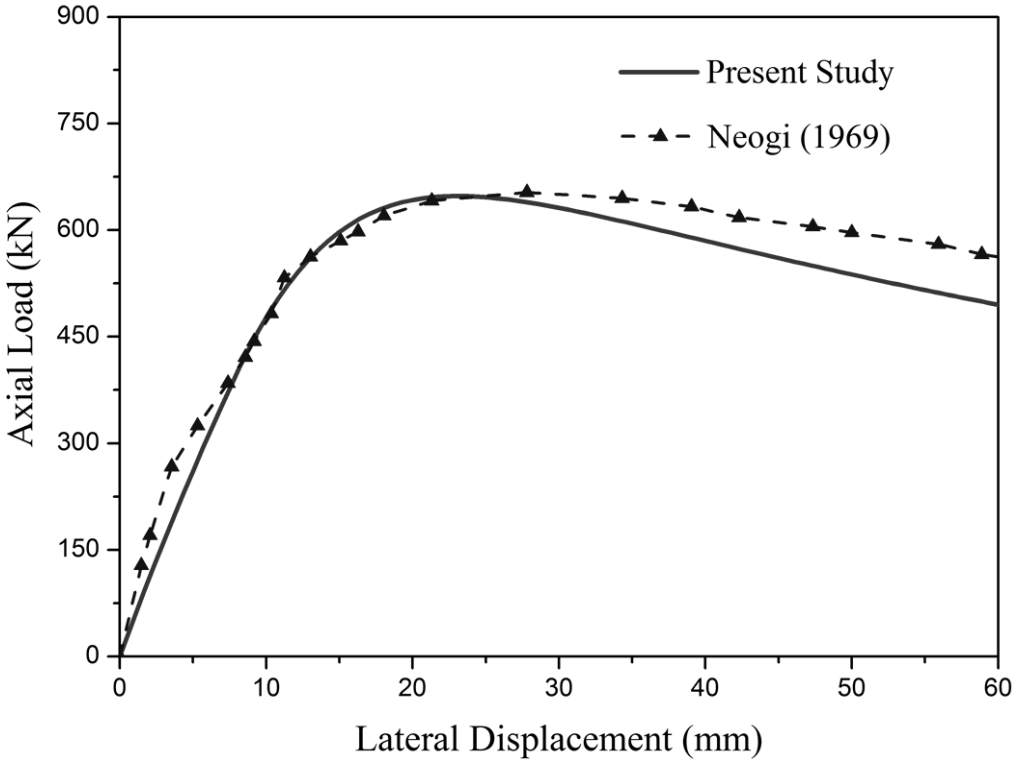

Fig. 24 Comparison between experiment and the present theory for member M5

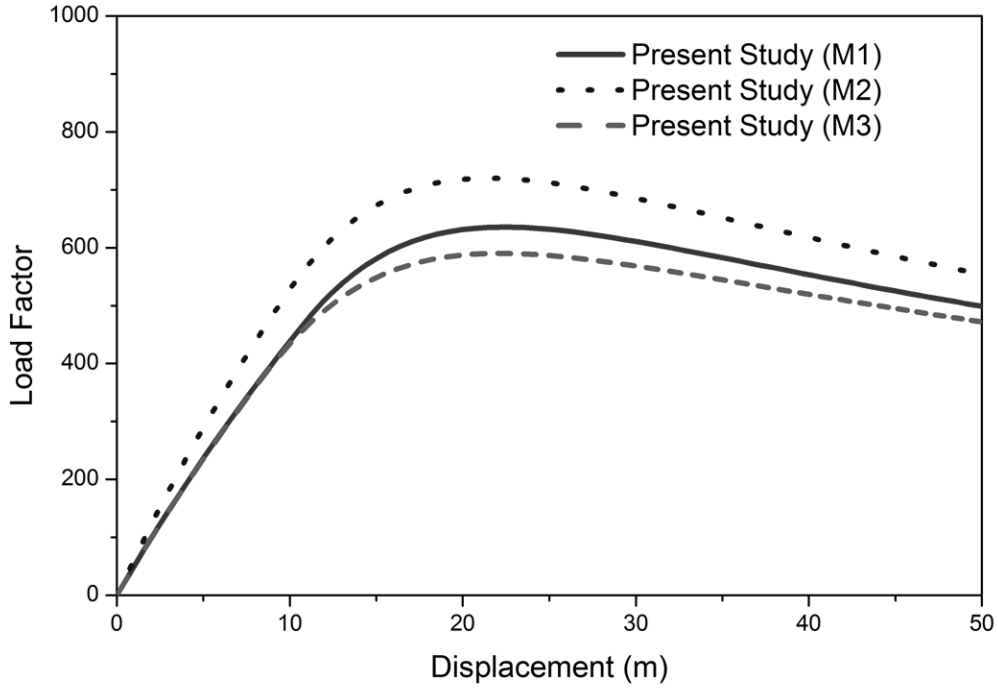

Fig. 25 Results by present theory for columns M1 to M3

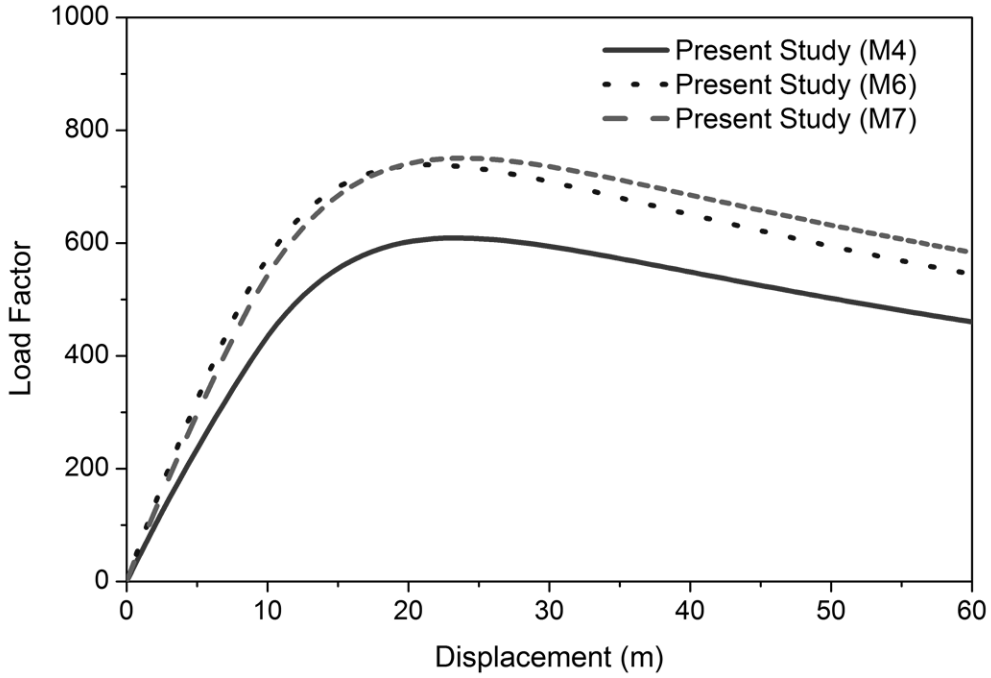

Fig. 26 Results by present theory for columns M4, M6 and M7

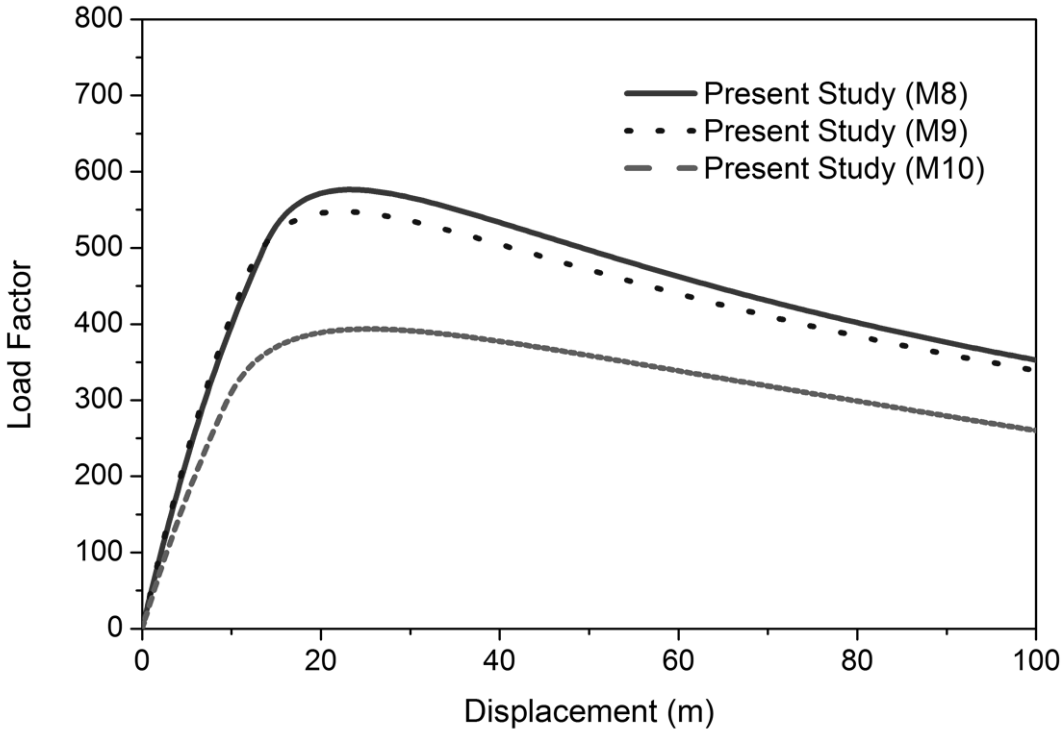

Fig. 27 Results by present theory for columns M8 to M10